

Assessing the potential of Jacobian-free Newton-Krylov methods for cell-centred finite volume solid mechanics

Philip Cardiff^{1,2,3*}, Ivan Batistić⁴ and Željko Tuković⁴

¹*School of Mechanical and Materials Engineering, University College Dublin, Ireland.

²UCD Centre for Mechanics, University College Dublin, Ireland.

³SFI I-Form Centre, University College Dublin, Ireland.

⁴Faculty of Mechanical Engineering and Naval Architecture, University of Zagreb, Croatia.

*Corresponding author. E-mail: philip.cardiff@ucd.ie

Abstract

In this study, we explore the efficacy of Jacobian-free Newton-Krylov methods within the context of finite-volume solid mechanics. Traditional Newton-based approaches to solving nonlinear systems typically require explicit formation and storage of the Jacobian matrix, which can be computationally expensive and memory-intensive. The Jacobian-free Newton-Krylov method circumvents this by employing Krylov subspace iterative solvers, such as GMRES, in conjunction with a Newton iteration scheme that approximates the action of the Jacobian through finite difference evaluations. A further potential advantage of the Jacobian-free Newton-Krylov method is that it is readily applicable to existing segregated finite volume frameworks, where forming and storing the exact Jacobian would require major code refactoring. This article research systematically evaluates the performance of Jacobian-free Newton-Krylov methods by benchmarking them against conventional segregated methods on a suite of benchmark cases of varying geometric dimension, geometric nonlinearity, dynamic response, and material behaviour. Key metrics such as computational cost, memory and robustness are analysed. Additionally, we investigate the impact of various solution algorithm choices, such as preconditioning strategy, on the efficiency of the Jacobian-free Newton-Krylov method. Our findings indicate that Jacobian-free Newton-Krylov methods can achieve comparable/superior/XXX convergence behaviour relative to traditional segregated methods, particularly in cases where YYYY. Summarise key findings: time, memory, important choices, JFNK vs SEG vs FE, ... The results suggest that Jacobian-free Newton-Krylov methods are promising for advancing finite-volume solid mechanics simulations and are particularly attractive for existing segregated frameworks where minimal code changes would be required to exploit openly available Jacobian-free Newton-Krylov implementations. The described implementations are made publicly available in the solids4foam toolbox for OpenFOAM, allowing the community to examine, extend and compare the procedures with the our codes.

1 Introduction

Finite volume formulations for solid mechanics are heavily influenced by their fluid mechanics counterparts, favouring segregated implicit and fully explicit methods. Segregated approaches, where the governing momentum equation is temporarily decomposed into scalar component equations, offer memory efficiency and simplicity of implementation, but the outer coupling Picard iterations often suffer from slow convergence. Explicit formulations are straightforward to implement and offer superior robustness but are only efficient for high-speed dynamics, where the physics requires small time increments. In contrast, the finite element community commonly employs Newton-Raphson-type solution algorithms, which necessitate repeated assembly of the Jacobian matrix and solution of the resulting block-coupled non-diagonally dominant linear system. A disadvantage of traditional Newton-based approaches is that they typically require explicit formation and storage of the Jacobian matrix, which can be computationally expensive and memory-intensive. A further disadvantage from a finite volume perspective is that extending existing code frameworks from segregated algorithms to a coupled Newton-Raphson-type approach is challenging in terms of the required assembly, storage, and solution of the resulting block-coupled system. In addition, the derivation of the true Jacobian matrix is non-trivial. Consequently, similar block-coupled solution finite volume methods are rare in the literature [1–3]. The motivation of the current work is to seek (or exceed) the robustness and efficiency of block-coupled Newton-Raphson approaches in a way that can be easily incorporated into existing segregated solution frameworks. To this end, the current article examines the efficacy of *Jacobian-free* Newton-Krylov methods, where the quadratic convergence of Newton methods can potentially be achieved without deriving, assembling and storing the exact Jacobian.

Jacobian-free Newton-Krylov methods circumvent the need for the Jacobian matrix by combining the Newton-Raphson method with Krylov subspace iterative linear solvers, such as GMRES, and noticing that such Krylov solvers do not explicitly require the Jacobian matrix. Instead, only the action of the Jacobian matrix on a solution-type vector is required. The key step in Jacobian-free Newton-Krylov methods is the approximation of products between the Jacobian matrix and a vector using the finite difference method; that is

$$\mathbf{J}\mathbf{v} \approx \frac{\mathbf{F}(\mathbf{x} + \epsilon\mathbf{v}) - \mathbf{F}(\mathbf{x})}{\epsilon} \quad (1)$$

where \mathbf{J} is the Jacobian matrix, \mathbf{x} is the current solution vector (e.g. nodal displacements), \mathbf{v} is a vector (e.g., from a Krylov subspace), and ϵ is a small scalar perturbation. With an appropriate choice of ϵ (balancing truncation and round-off errors), the characteristic quadratic convergence of Newton methods can be achieved without the Jacobian, hence the modifier *Jacobian-free*. This approach promises significant memory savings over Jacobian-based methods, especially for large-scale, but also potentially for execution time, with appropriate choice of solution components.

A crucial aspect of ensuring the efficiency and robustness of the Jacobian-free Newton-Krylov method is the choice of a suitable preconditioner for the Krylov iterations. This preconditioner is often derived from the exact Jacobian matrix in traditional Newton methods. However, the Jacobian-free approach does not allow direct access to the full Jacobian matrix, necessitating an alternative strategy to approximate its action. To this end, and to extend existing segregated frameworks, we propose using a compact-stencil approximate Jacobian as the preconditioner. This approximate Jacobian corresponds to the matrix typically employed in segregated approaches; similar approaches are successful in fluid mechanics applications [4?]; however, it is unclear if such an approach is suitable for solid mechanics - a question which we hope to answer in this work. By leveraging this compact-stencil approximate Jacobian, we aim to effectively precondition the Krylov iterations, enhancing convergence while maintaining the memory and computational savings that define the Jacobian-free and segregated methods. Similarly, if such an approach is efficient, it would naturally fit into existing segregated frameworks, as existing matrix storage and assembly can be reused.

The remainder of the paper is structured as follows: Section 2 summarises a typical solid mechanics mathematical model and its cell-centred finite volume discretisation. Section 3 presents the solution algorithms, starting with the classic segregated solution algorithm, followed by the proposed Jacobian-free Newton-Krylov solution algorithm. The performance of the proposed Jacobian-free Newton-Krylov approach is compared with the segregated approach on several varying benchmark cases in Section 4, where the effect of several factors are examined, including problem dimension, mesh, material model, nonlinear geometry, choice of preconditioner, and other solution parameter. Finally, the article ends with a summary of the main conclusions of the work.

2 Mathematical Model and Numerical Methods

2.1 Governing Equations

In this work, we restrict our interest to Lagrangian formulations of the conservation of linear momentum. Assuming small strains, the linear geometry formulation is expressed in strong integral form as:

$$\int_{\Omega} \rho \frac{\partial^2 \mathbf{u}}{\partial t^2} d\Omega = \oint_{\Gamma} \mathbf{n} \cdot \boldsymbol{\sigma}_s d\Gamma + \int_{\Omega} \mathbf{f}_b d\Omega \quad (2)$$

where Ω is the volume of an arbitrary body bounded by a surface Γ with outwards pointing normal \mathbf{n} . The density is ρ , \mathbf{u} is the displacement vector, $\boldsymbol{\sigma}_s$ is the engineering (small strain) stress tensor, and \mathbf{f}_b is a body force per unit volume, e.g., $\rho \mathbf{g}$, where \mathbf{g} is gravity.

More generally, linear momentum conservation can be expressed in a nonlinear geometry form, which is suitable for finite strains. Two equivalent nonlinear geometry forms are common: the *total* Lagrangian form:

$$\int_{\Omega_o} \rho_o \frac{\partial^2 \mathbf{u}}{\partial t^2} d\Omega_o = \oint_{\Gamma_o} (\mathbf{J} \mathbf{F}^{-T} \cdot \mathbf{n}_o) \cdot \boldsymbol{\sigma} d\Gamma_o + \int_{\Omega_o} \mathbf{f}_b d\Omega_o \quad (3)$$

and the *updated* Lagrangian form:

$$\int_{\Omega_u} \frac{\partial}{\partial t} \left(\rho_u \frac{\partial \mathbf{u}}{\partial t} \right) d\Omega_u = \oint_{\Gamma_u} (j \mathbf{f}^{-T} \cdot \mathbf{n}_u) \cdot \boldsymbol{\sigma} d\Gamma_u + \int_{\Omega_u} \mathbf{f}_b d\Omega_u \quad (4)$$

where subscript o indicates quantities in the initial reference configuration, and subscript u indicates quantities in the updated configuration. The true (Cauchy) stress tensor is indicated by $\boldsymbol{\sigma}$.

The deformation gradient is defined as $\mathbf{F} = \mathbf{I} + (\nabla \mathbf{u})^T$ and its determinant as $J = \det(\mathbf{F})$. Similarly, the *relative* deformation gradient is given in terms of the displacement *increment* as $\mathbf{f} = \mathbf{I} + [\nabla(\Delta \mathbf{u})]^T$ and its determinant as $j = \det(\mathbf{f})$. The displacement increment is the change in displacement between the current time step and the previous time step when the time interval is discretised into a finite number of steps.

The definition of the engineering stress ($\boldsymbol{\sigma}_s$) and true stress ($\boldsymbol{\sigma}$) in Equations 2, 3 and 4 is given by a chosen mechanical law, e.g. linear elasticity. Several mechanical laws are considered in this work, as briefly described in Section 4.

2.2 Newton-Type Solution Methods

To facilitate the comparison between classic segregated solution algorithms and the proposed Jacobian-free Newton-Krylov algorithm, the governing linear momentum conservation (Equations 2, 3 and 4) is expressed in the general form:

$$\mathcal{R}(\mathbf{u}) = \mathbf{0} \quad (5)$$

where \mathcal{R} represents the *residual* (imbalance) of the equation, which is a function of the primary unknown field. For example, in the linear geometry case, the residual is given as

$$\mathbf{R}(\mathbf{u}) = \oint_{\Gamma} \mathbf{n} \cdot \boldsymbol{\sigma}_s(\mathbf{u}) d\Gamma + \int_{\Omega} \rho \mathbf{g} d\Omega - \int_{\Omega} \rho \frac{\partial^2 \mathbf{u}}{\partial t^2} d\Omega = \mathbf{0} \quad (6)$$

where the dependence of the stress tensor on the solution vector is made explicitly clear: $\boldsymbol{\sigma}_s(\mathbf{u})$.

In Newton-type methods, a Taylor expansion about a current point \mathbf{u}_k can be used to solve Equation 5 [5]:

$$\mathbf{R}(\mathbf{u}_{k+1}) = \mathbf{R}(\mathbf{u}_k) + \mathbf{R}'(\mathbf{u}_k)(\mathbf{u}_{k+1} - \mathbf{u}_k) + \text{H.O.T.} = \mathbf{0} \quad (7)$$

Neglecting the higher-order terms (H.O.T.) yields the strict Newton method in terms of an iteration over a sequence of linear systems:

$$\begin{aligned} \mathbf{J}(\mathbf{u}_k) \delta \mathbf{u} &= -\mathbf{R}(\mathbf{u}_n), \\ \mathbf{u}_{k+1} &= \mathbf{u}_k + s \delta \mathbf{u}, \\ k &= 0, 1, \dots \end{aligned} \quad (8)$$

where $\mathbf{J} \equiv \mathbf{R}'$ is the Jacobian matrix. Starting the Newton procedure requires the specification of \mathbf{u}_0 . The scalar $s > 0$ can be chosen to improve convergence, for example, using a line search or under-relaxation procedure, and is equal to unity in the classic Newton-Raphson approach. Iterations are performed over this system until the residual $\mathbf{R}(\mathbf{u}_n)$ and solution correction $\delta\mathbf{u}$ are sufficiently small, with appropriate normalisation.

For problems with N scalar equations and N scalar unknowns, the residual \mathbf{R} and solution \mathbf{u} vectors have dimensions of $N \times 1$. The components of the $N \times N$ Jacobian are

$$J_{ij} = \frac{\partial R_i(\mathbf{u})}{\partial u_j} \quad (9)$$

In the current work, we are interested in vector problems, where the governing momentum equation is formulated in terms of the unknown displacement solution vector. In this case, Equation 9 refers to the individual scalar components of the residual, solution, and Jacobian. That is, for 3-D analyses, the residual takes the form

$$\mathbf{R}(\mathbf{u}) = \{R_1^x, R_1^y, R_1^z, R_2^x, R_2^y, R_2^z, \dots, R_n^z\} \quad (10)$$

and the solution takes the form

$$\mathbf{u} = \{u_1^x, u_1^y, u_1^z, u_2^x, u_2^y, u_2^z, \dots, u_n^z\} \quad (11)$$

In practice, it is often more practical and efficient to form and store the residual, solution and Jacobian in a *blocked* manner, where the residual and solution can be considered as vectors of vectors. Similarly, the Jacobian can be formed in terms of sub-matrix block coefficients.

In the strict Newton procedure, the residuals converge at a quadratic rate when the current solution is close to the true solution; that is, the iteration error decreases proportionally to the square of the error at the previous iteration. Once the method gets sufficiently close to the true solution, the number of correct digits in the approximation roughly doubles with each iteration. However, quadratic convergence is only possible when using the exact Jacobian. In contrast, a quasi-Newton method uses an approximation to the Jacobian, sacrificing strict quadratic convergence in an attempt to produce an overall more computationally efficient procedure. From this perspective, the segregated solution algorithm commonly employed in finite volume solid mechanics can be viewed as a quasi-Newton method, where an approximate Jacobian replaces the exact Jacobian:

$$\tilde{\mathbf{J}}(\mathbf{u}_k) \delta\mathbf{u} = -\mathbf{R}(\mathbf{u}_k) \quad (12)$$

In this case, the approximate Jacobian $\tilde{\mathbf{J}}$ comes from the compact stencil discretisation of a simple diffusion (Laplacian) term. A benefit of this approach is that the inter-component coupling is removed from the Jacobian, allowing the solution of three smaller scalar systems rather than one larger vector system in 3-D (or two smaller systems in 2-D).

A fully explicit procedure can also be viewed from this perspective by selecting an approximate Jacobian, which is diagonal $\tilde{\mathbf{D}}$, making the solution of the linear system trivial:

$$\tilde{\mathbf{D}}(\mathbf{u}_k) \delta\mathbf{u} = -\mathbf{R}(\mathbf{u}_k) \quad (13)$$

2.3 Cell-Centred Finite Volume Discretisation

In this work, a nominally second-order cell-centred finite volume discretisation is employed, as described previously, for example, [6–9]. Consequently, only a summary of the discretisation is presented below.

The solution domain is discretised in both space and time. The total simulation period is divided into a finite number of time increments, denoted as Δt , and the discretised governing momentum equation is solved iteratively in a time-marching fashion. The spatial domain is partitioned into a finite number of contiguous convex polyhedral cells.

The conservation equation (Equations 2, 3, or 4) is applied to each cell (control volume) in the computational mesh and discretised in terms of the displacement at the cell centre/centroid \mathbf{u}_P and at the centres of the neighbouring cells N_i .

To complete the discretisation, the volume integrals and surface integrals in the governing equation must be approximated by algebraic equations. Starting first with the volume integrals, assuming a linear variation of the integrand, the mid-point rule approximates the integral in terms of the cell centre value. Consequently, the inertia term (e.g. left-hand side term of Equation 2) becomes

$$\int_{\Omega} \rho \frac{\partial \mathbf{u}}{\partial t} d\Omega \approx \rho_P \left(\frac{\partial^2 \mathbf{u}}{\partial t^2} \right)_P \Omega_P \quad (14)$$

and, similarly, the body force term (e.g. the second term on the right-hand side of Equation 2) becomes:

$$\int_{\Omega} \rho \mathbf{g} d\Omega \approx \rho_P \mathbf{g} \Omega_P \quad (15)$$

where subscript P indicates a quantity at the cell centre. The discretisation of the acceleration in time in Equation 14 can be achieved using the finite difference method, e.g. first-order Euler, second-order backwards, second-order Newmark-beta. Maybe we should give the temporal discretisation for completeness: i.e. 2nd order backwards

The surface integral term (e.g. first term on the right-hand side of Equation 2), corresponding to the divergence of stress, is discretised by assuming that the stress varies linearly across the face, allowing the mid-point rule to be used:

$$\oint_{\Gamma} \mathbf{n} \cdot \boldsymbol{\sigma} d\Gamma \approx \sum_{f \in N_f} \mathbf{\Gamma}_f \cdot \boldsymbol{\sigma}_f \quad (16)$$

where subscript f indicates a quantity at the centre of a cell face, and N_f represents the set of neighbouring cells which share a face with cell P . The stress at a face, σ_f , is calculated by linearly interpolating from the adjacent cell centres. Stress is calculated at the cell centres as a function of the displacement gradient, $(\nabla \mathbf{u})_f$, and the cell-centre gradients are determined using a least squares method [?].

The discretisation is complete but, in its current form, is known to suffer from zero-energy modes, i.e. checkerboarding oscillations. Here, a Rhie-Chow-type stabilisation term [10] is added to the residual (Equation 5) to quell such oscillations. The Rhie-Chow stabilisation term, first used for finite volume solid mechanics by Demirdžić and Muzaferija [11], consists of the numerical difference between a diffusion (Laplacian) term calculated using compact and larger computational stencils. The term introduces numerical diffusion to the discretisation, which reduces at a third-order rate. In the current approach, the Rhie-Chow stabilisation term $\mathcal{D}_{\text{Rhie-Chow}}$ for a cell P takes the following form:

$$\mathcal{D}_{\text{Rhie-Chow}} = \sum_{f \in N_f} \alpha \bar{K}_f \left[|\Delta_f| \frac{\mathbf{u}_{N_f} - \mathbf{u}_P}{|\mathbf{d}_f|} - \Delta_f \cdot (\nabla \mathbf{u})_f \right] |\Gamma_f| \quad (17)$$

where $\alpha > 0$ is a user-defined parameter for globally scaling the amount of stabilisation. Parameter \bar{K}_f is a stiffness-type parameter that gives the stabilisation an appropriate scale and dimension. Here, $\bar{K}_f = \frac{4}{3}\mu + \kappa = 2\mu + \lambda$ following previous work [? ? ?], where μ is the shear modulus (first Lamé parameter), κ is the bulk modulus, and λ is the second Lamé parameter. Vector \mathbf{d}_f connects cell centre P with the other cell sharing face f , and \mathbf{n}_f is the outward-facing unit normal to the face f . The vector $\Delta_f = \frac{\mathbf{d}_f}{\mathbf{d}_f \cdot \mathbf{n}_f}$ is termed the *over-relaxed orthogonal* vector [12] and increases in magnitude as the deviation between the \mathbf{d}_f and \mathbf{n}_f vectors increases. In this way, the amount of stabilisation increases on distorted meshes. Should we mention Nishikawa alpha scheme? Very similar: but scales differently with mesh distortion

In Equation 17, the first term within the brackets on the right-hand side represents a compact stencil (two-node) approximation of the face normal gradient, while the second term represents a larger stencil approximation. These two terms cancel out in the limit of mesh refinement (or if the solution varies linearly); otherwise, they produce a stabilisation effect that tends to smooth the solution fields. As the term reduces at a third-order rate, it does not affect the overall scheme's second-order accuracy.

All dependent variables must be specified at the initial time. Boundary conditions must be applied to the faces that coincide with the boundary of the solution domain. The discretised expressions on boundary faces are modified to account for either the known displacement components in Dirichlet conditions or the known traction for Neumann conditions.

Comment on traction boundaries extrapolate to get value or use constitutive law

3 Solution Algorithms

3.1 Segregated Solution Algorithm

The classic segregated solution algorithm can be viewed as a quasi-Newton method, where a compact-stencil approximation of a diffusion term is employed as the approximate Jacobian:

$$\begin{aligned}\tilde{\mathbf{J}} &= \oint_{\Gamma} \bar{K} \mathbf{n} \cdot \nabla \mathbf{u} d\Gamma \\ &\approx \sum_{f \in N_f} \bar{K}_f |\Delta_f| \left(\frac{\mathbf{u}_{N_f} - \mathbf{u}_P}{|d_f|} \right) |\Gamma_f|\end{aligned}\quad (18)$$

When a diffusion term is typically discretised using the cell-centre finite volume method, non-orthogonal corrections are included in a deferred correction manner to preserve the order of accuracy on distorted grids. However, in the Newton method case, the approximate Jacobian's exact value does not affect the final converged solution, but only the convergence behaviour. Consequently, non-orthogonal corrections are not included in the approximate Jacobian here. However, grid distortion is appropriately accounted for in the calculation of the residual. Nonetheless, as a result, it is expected that the convergence behaviour of the segregated approach may degrade as mesh non-orthogonality increases.

The linearised system (Equation 12) is formed for each cell in the domain, resulting in a system of algebraic equations:

$$\tilde{\mathbf{J}}(\mathbf{u}_n) \delta \mathbf{u} = -\mathbf{R}(\mathbf{u}_n) \quad (19)$$

where $\tilde{\mathbf{J}}$ is a symmetric, weakly diagonally dominant, $M \times M$ stiffness matrix, where M is three times the number of cells in 3-D and twice the number of cells in 2-D. By design, matrix $\tilde{\mathbf{J}}$ contains no inter-component coupling; consequently, three equivalent smaller linear systems can be formed and solved for the Cartesian components of the displacement correction (or two in 2-D), e.g.

$$\tilde{\mathbf{J}}_x(\mathbf{u}_n) \Delta \mathbf{u}_x = -\mathcal{R}_x(\mathbf{u}_n) \quad (20)$$

$$\tilde{\mathbf{J}}_y(\mathbf{u}_n) \Delta \mathbf{u}_y = -\mathcal{R}_y(\mathbf{u}_n) \quad (21)$$

$$\tilde{\mathbf{J}}_z(\mathbf{u}_n) \Delta \mathbf{u}_z = -\mathcal{R}_z(\mathbf{u}_n) \quad (22)$$

where \bullet_x represents the components in the x direction, \bullet_y represents the components in the y direction, and \bullet_z represents the components in the z direction. An additional benefit of the segregated approach, from a memory perspective, is that matrices $\tilde{\mathbf{J}}_x$, $\tilde{\mathbf{J}}_y$ and $\tilde{\mathbf{J}}_z$ are identical, except for the effects from including boundary conditions. From an implementation perspective, this allows a single scalar matrix to be formed and stored, where the boundary condition contributions are inserted before solving a particular component.

The *inner* linear sparse systems (Equations 20, 21 and 22) can be solved using any typical direct or iterative linear solver approach; however, an incomplete Cholesky pre-conditioned conjugate

gradient method [13] is often preferred as the weakly diagonally dominant characteristic leads to good convergence characteristics. Algebraic multigrid can be used to accelerate convergence.

In literature, the segregated solution algorithm is typically formulated in terms of the total displacement vector (or its difference between time steps) as the primary unknown; in contrast, in the quasi-Newton interpretation presented here, the primary unknown is the correction to the displacement vector, which goes to zero at convergence. Nonetheless, both approaches are equivalent and neither formulation displays superior performance.

The current procedure is implemented and publicly shared in the solids4foam toolbox of OpenFOAM. Add a section about code sharing: appendix?

Comment: we have two implementations of segregated: native OpenFOAM (solves Eqs 16-18) and PETSc SNES (solves Eq 15) Do we need to comment on this? Maybe we should use only PETSc SNES for a fair comparison Or we could use both on the verification case and then stick with just one afterwards

3.2 Jacobian-free Newton-Krylov Algorithm

As noted in the introduction, the Jacobian-free Newton-Krylov avoids the need to construct the Jacobian matrix explicitly by approximating its action on a solution vector using the finite difference method, repeated here:

$$\mathbf{J}\mathbf{v} \approx \frac{\mathbf{F}(\mathbf{x} + \epsilon\mathbf{v}) - \mathbf{F}(\mathbf{x})}{\epsilon} \quad (23)$$

The derivation of this approximation can be shown for a 2×2 system as [5]:

$$\begin{aligned} \frac{\mathbf{F}(\mathbf{x} + \epsilon\mathbf{v}) - \mathbf{F}(\mathbf{x})}{\epsilon} &= \left(\begin{array}{c} \frac{F_1(x_1 + \epsilon v_1, x_2 + \epsilon v_2) - F_1(x_1, x_2)}{\epsilon} \\ \frac{F_2(x_1 + \epsilon v_1, x_2 + \epsilon v_2) - F_2(x_1, x_2)}{\epsilon} \end{array} \right) \\ &\approx \left(\begin{array}{c} \frac{F_1(x_1, x_2) + \epsilon v_1 \frac{\partial F_1}{\partial u_1} + \epsilon v_2 \frac{\partial F_1}{\partial u_2} - F_1(x_1, x_2)}{\epsilon} \\ \frac{F_2(x_1, x_2) + \epsilon v_1 \frac{\partial F_2}{\partial u_1} + \epsilon v_2 \frac{\partial F_2}{\partial u_2} - F_2(x_1, x_2)}{\epsilon} \end{array} \right) \\ &\approx \left(\begin{array}{c} v_1 \frac{\partial F_1}{\partial u_1} + v_2 \frac{\partial F_1}{\partial u_2} \\ v_1 \frac{\partial F_2}{\partial u_1} + v_2 \frac{\partial F_2}{\partial u_2} \end{array} \right) \\ &\approx \mathbf{J}\mathbf{v} \end{aligned} \quad (24)$$

where a first-order truncated Taylor series expansion about \mathbf{u} was used to approximate $\mathbf{F}(\mathbf{x} + \epsilon\mathbf{v})$. As noted above, choosing an appropriate value for ϵ is non-trivial, and care must be taken to balance truncation error (reduced by decreasing ϵ) and round-off error (increased by decreasing ϵ).

The purpose of preconditioning the Jacobian-free Newton-Krylov method is to reduce the number of inner linear solver iterations. In the current work, the GMRES linear solver is used for the inner system. Using right preconditioning, the finite difference approximation of Equation 23

becomes

$$\mathbf{J}\mathbf{P}^{-1}\mathbf{v} \approx \frac{\mathbf{F}(\mathbf{x} + \epsilon\mathbf{P}^{-1}\mathbf{v}) - \mathbf{F}(\mathbf{x})}{\epsilon} \quad (25)$$

where \mathbf{P} is the preconditioning matrix or process. In practice, only the action of \mathbf{P}^{-1} on a vector is required, and the \mathbf{P}^{-1} may not be explicitly formed. Concretely, the preconditioner needs to approximately solve the linear system $\mathbf{y} = \mathbf{P}^{-1}\mathbf{v}$.

In the current work, we proposed to use the compact-stencil approximate Jacobian from the segregated algorithm $\tilde{\mathbf{J}}$ as the preconditioning matrix \mathbf{P} for the preconditioned Jacobian-free Newton-Krylov method. **Comment on literature: used before but not yet for solids.** This preconditioning approach can be considered as a “physics-based” preconditioner in the classifications of [5]. The approach is conceptually similar to an approximation of the Jacobian of a higher-order advection scheme by a compact-stencil lower-order upwind scheme. A benefit of the proposed approach is that existing segregated frameworks can re-use their existing discretisation and storage implementations. Concretely, the Jacobian-free Newton-Krylov method requires only a procedure for forming this preconditioning matrix and a procedure for explicitly evaluating the residual. Both routines are easily implemented in an existing segregated framework. The only additional required procedure is an interface to an existing Jacobian-free Newton-Krylov implementation. In the current work, the PETSc toolbox [14] is used as the nonlinear solver, where driven by a finite volume solver in the OpenFOAM toolbox [?].

Several preconditioners are available in the literature, incomplete Cholesky/LU being popular; however, multigrid methods offer the greatest potential for large-scale problems. Knoll and Keyes [5] noted that algorithmic simplifications within a multigrid procedure, which may result in loss of convergence for multigrid as a solver, have a much weaker effect when multigrid is the preconditioner. In this work, three preconditioners are considered:

1. ILU(N): incomplete LU with fill-in N . The segregated solver uses ILU(0), that is, ILU with zero fill-in.
2. Multigrid: here, we use the HYPRE Boomerang multigrid implementation.
3. LU: for comparison, we consider a direct LU decomposition solver as the preconditioner.

A challenge with Newton-type methods, including Jacobian-free versions, is convergence can be poor when far from the true solution, and divergence is often a real possibility. Globalisation refers to steering an initial solution towards the quadratic convergence range of the Newton method. Several strategies are possible, and it is common to combine approaches [5]. In the current work, a line search procedure is used to select the s parameter in the solution update step (the second line in Equations 8). Line search methods assume the Newton update direction is correction and aim to find a scalar $s > 0$ that decreases the residual $\mathbf{R}(\mathbf{u}_k + s\delta\mathbf{u}) < \mathbf{R}(\mathbf{u}_k)$. The scalar s is typically ≤ 1 , but extrapolation (> 1) is also possible for accelerating convergence, albeit at the expense of robustness.

In addition to a line search approach, a *transient continuation* globalisation approach is used in the current work, where a prediction for the solution (displacement) field at time $t + \Delta t$ is performed

at the start of a new time step, based on a truncated second-order Taylor series expansion:

$$\mathbf{u}_{t+\Delta t} = \mathbf{u}_t + \Delta t \left(\frac{\partial \mathbf{u}}{\partial t} \right)_t + \frac{1}{2} \Delta t^2 \left(\frac{\partial^2 \mathbf{u}}{\partial t^2} \right)_t \quad (26)$$

where Δt is the time increment (assumed constant here), $\left(\frac{\partial \mathbf{u}}{\partial t} \right)_t$ is the velocity at time t , and $\left(\frac{\partial^2 \mathbf{u}}{\partial t^2} \right)_t$ is the acceleration at time t . In this way, for highly nonlinear problems, the user can decrease the time step size Δt as a globalisation approach to improve the performance of the Newton method. The predictor step in Equation 26 has been chosen to be consistent with the assumed discretisation of the temporal term in the governing equation; that is, the second order backwards scheme is assumed.

A final comment on the Jacobian-free Newton-Krylov solution algorithm is the potential importance of *oversolving*. Here, oversolving refers to solving the linear system to too tight a tolerance during the early Newton iterations, essentially wasting time when the solution is far from the true solution. In addition, some authors [5] have shown Newton convergence to be worse when the earlier iterations are solved to too tight a tolerance. The concept of oversolving also applies to segregated solution procedures and has been well-known since the early work of Demirdžić and co-workers [?], where the residuals are typically reduced by one order of magnitude in the inner linear system. The optimal choice of residual reduction for a Jacobian-free Newton-Krylov finite volume solid mechanics procedure is explored in Section 4. Check: do we examine this?

4 Test Cases

This section assesses the performance of the proposed Jacobian-free Newton-Krylov solution approach on several benchmark cases. The cases have been chosen to exhibit a variety of characteristics in terms of

- Geometric dimension (2-D vs. 3-D),
- Geometric nonlinearity (small strain vs. large strain),
- Geometric complexity (basic geometric shapes vs. complex geometry),
- Statics vs. dynamics, and
- Material behaviour (elasticity, elastoplasticity, hyperelasticity).

In addition, through the analysis of the benchmark cases above, the effect of several parameters will be examined, including the mesh types, Rhie-Chow stabilisation scaling, preconditioner choices, linear solver settings, the effect of globalisation strategies, and multi-CPU-core parallelisation. The performance of the Jacobian-free Newton-Krylov algorithm is compared with that of the segregated algorithm in terms of computational time and memory requirements. In all cases, the residuals are dropped by six orders of magnitude unless stated otherwise. Metrics from a commercial finite element software (Abaqus) are included for reference ask Dylan to run Abaqus cases once we have our results.

The presented analyses aim to be extensive but not exhaustive. Several common features of modern solid mechanics procedures are left for future work, including contact mechanics and incompressibility.

The remainder of this section is structured as follows: The proposed discretisation's accuracy and order are assessed on several test cases of varying dimensions and phenomena. Subsequently, the remaining sub-sections assess the efficiency of the Jacobian-free Newton-Krylov approach compared with the standard segregated procedure and, in some cases, finite element solutions.

4.1 Testing the Accuracy and Order of Accuracy

This section solely focuses on assessing the accuracy and order of accuracy of the discretisation. Assessment of the computational efficiency regarding time and memory requirements is left to the subsequent sections.

Case 1: Order Verification via the Manufactured Solution Procedure

The first test case consists of a $0.2 \times 0.2 \times 0.2$ m cube with linear elastic ($E = 200$ GPa, $\nu = 0.3$) properties. A manufactured solution for displacement (Figure 1(a)) is employed of the form:

$$\mathbf{u} = \begin{pmatrix} a_x \sin(4\pi x) \sin(2\pi y) \sin(\pi z) \\ a_y \sin(4\pi x) \sin(2\pi y) \sin(\pi z) \\ a_z \sin(4\pi x) \sin(2\pi y) \sin(\pi z) \end{pmatrix} \quad (27)$$

where $a_x = 2 \times 10^{-6}$ m, $a_y = 4 \times 10^{-6}$ m, and $a_z = 6 \times 10^{-6}$ m. The Cartesian coordinates are given by x , y and z . The corresponding manufactured body force term is given in Appendix B.

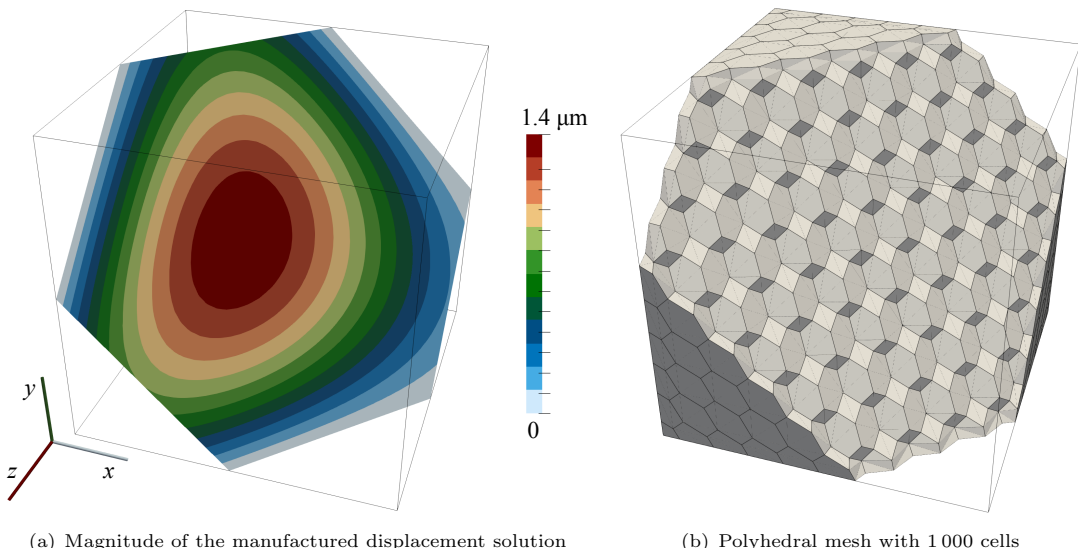


Fig. 1 A cut plane through the cube case geometry showing the magnitude of the manufactured displacement solution (left) and a polyhedral mesh with 1 000 cells. The cut plane passes through the centre of the cube and has the unit normal $\mathbf{n} = (1/\sqrt{3} \quad 1/\sqrt{3} \quad 1/\sqrt{3})$.

The manufactured displacement solution is applied at the domain's boundaries, and inertial effects are neglected. Three mesh types are examined: (i) hexahedra, (ii) tetrahedra, and (iii) regular polyhedra (Figure 1(b)). The hexahedral meshes are created using the OpenFOAM `blockMesh` utility, while the tetrahedral meshes are created using Gmsh [15]. To create the polyhedral meshes, the tetrahedra meshes are converted to their dual polyhedral representations using the OpenFOAM `polyDualMesh` utility. Starting from an initial mesh spacing of 0.04 m, six meshes are created by successively halving the spacing. The cell numbers for the hexahedral and polyhedral meshes are 125, 1 000, 8 000, 64 000, 512 000, and 4 096 000, while the tetrahedral mesh cell counts are 384, 4 374, 41 154, 355 914, 2 958 234, and 24 118 074. For the same average cell width, the cell counts show that the tetrahedral meshes have larger cell counts by a factor of 3 to 6.

Figure 2(a) shows the displacement magnitude discretisation errors (L_2 and L_∞) as a function of the average cell width for all three mesh types (hexahedral, tetrahedral and polyhedral), while Figure 2(b) shows the corresponding order of accuracy plots. For ease of interpretation, the symbol shapes in the figures have been chosen to correspond to the cell shapes: a square for hexahedra, a triangle for tetrahedra and a pentagon for polyhedra. The maximum (L_∞) and average (L_2) discretisation errors are seen to reduce at an approximately second-order rate for all mesh types, except for the L_2 error on the hexahedral meshes, which is approximately 2.3 on the finest grid.

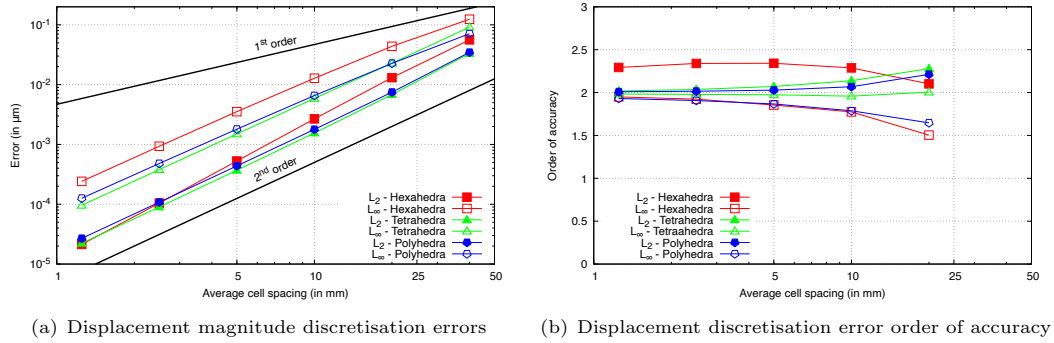


Fig. 2 Manufactured solution cube case: the accuracy and order of accuracy for displacement magnitude

The predicted σ_{xx} stress distribution for a hexahedral mesh with 512 000 cells is shown in Figure 3(a). The corresponding cell-wise σ_{xx} error distribution is shown in Figure 3(b). The errors of greatest magnitude (43 kPa) occur at the boundaries, corresponding to where the local truncation error is higher due to the use of one-sided differencing. The discretisation errors in the stress magnitude are shown in Figure 4(a), and the order of accuracy in Figure 4(b). The order of accuracy for the average (L_2) stress error is seen to be approximately 1.5 for the hexahedral and polyhedral meshes. In contrast, the average stress error order for the tetrahedral meshes is 1. Similarly, the maximum (L_∞) stress order of accuracy is seen to approach 1 for all three mesh types.

The presented results have been generated using the Jacobian-free Newton-Raphson solution algorithm; however, minimal differences were seen when using the segregated solution algorithm, and hence, the segregated results are not shown.

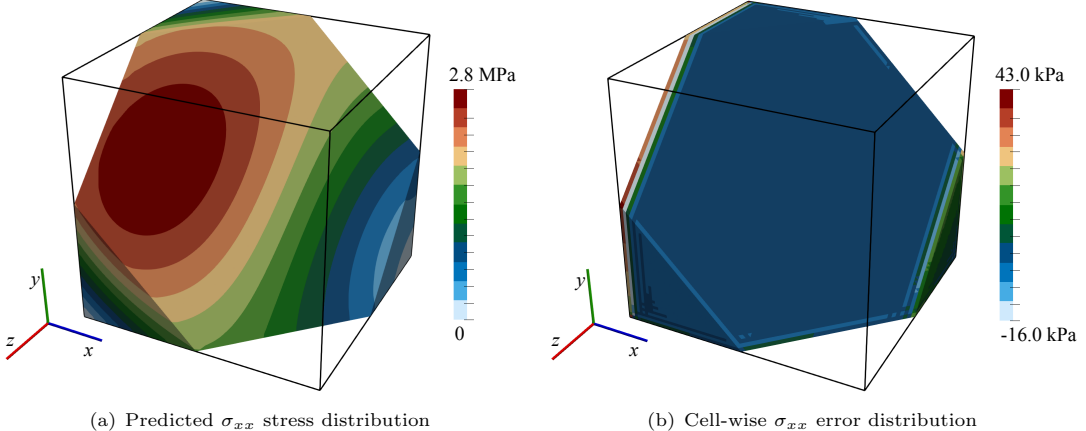


Fig. 3 Manufactured solution cube case: the predicted σ_{xx} stress distribution on a cut-plane for the hexahedral mesh with 512 000 cells (left).

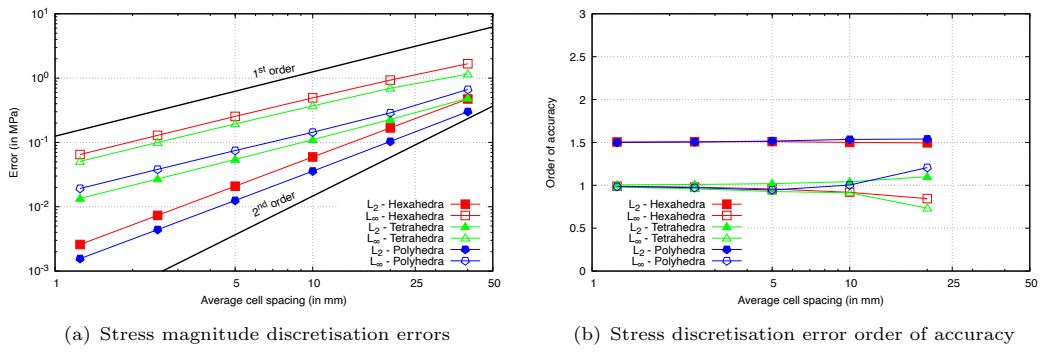


Fig. 4 Manufactured solution cube case: the accuracy and order of accuracy for stress magnitude

Case 1b: Spherical Cavity in an Infinite Solid Subjected to Remote Stress

This 3-D problem consists of a spherical cavity with radius $a = 0.2$ m (Figure 5) in an infinite, isotropic linear elastic solid ($E = 200$ GPa, $\nu = 0.3$). Far from the cavity, the solid is subjected to a tensile stress $\sigma_{zz} = T = 1$ MPa, with all other stress components zero. The analytical expressions

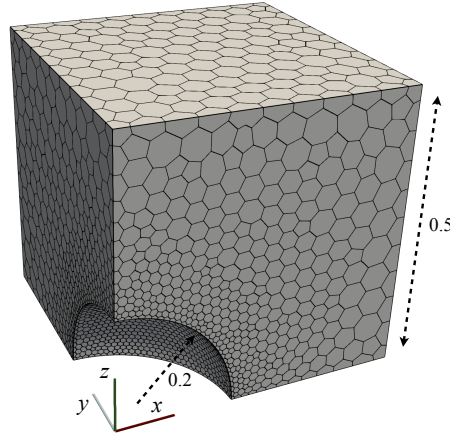


Fig. 5 Spherical cavity case geometry, showing the polyhedral mesh with 4 539

for the stress and displacement distributions are given in Appendix C.

The computational solution domain is taken as one-eighth of a $1 \times 1 \times 1$ m cube aligned with the Cartesian axes, with one corner at the centre of the sphere. The analytical tractions are applied at the far boundaries of the domain to mitigate the effects of finite geometry. Unstructured polyhedral meshes are employed with grading towards the cavity. The cell sizes at the cavity surfaces are 100, 50, 25, 12.5, 6.25, and 3.125 mm, and the corresponding cell counts are 976, 4552 (Figure 5), 29 611, 213 100, 614 261. Initially, unstructured tetrahedral meshes were generated using the Gmsh meshing utility [15], followed by conversion to their dual polyhedral representations using the OpenFOAM `polyDualMesh` utility.

The spherical cavity case errors seem to approach zero order accuracy. Maybe we have hit the precision limit...? We may leave this case out

Case 2: Out-of-plane bending of an elliptic plate

This 3-D, static, linear elastic test case (Figure 6) consists of a thick elliptic plate (0.6 m thick) with a centred elliptic hole, with the inner and outer ellipses given as

$$\left(\frac{x}{2}\right)^2 + \left(\frac{y}{1}\right)^2 = 1 \text{ inner ellipse} \quad (28)$$

$$\left(\frac{x}{3.25}\right)^2 + \left(\frac{y}{2.75}\right)^2 = 1 \text{ outer ellipse} \quad (29)$$

The case has been described by the National Agency for Finite Element Methods and Standards (NAFEMS) [16], and analysed using finite volume procedures by Demirdžić et al. [17] and Cardiff et al. [18]. Symmetry allows one-quarter of the geometry to be simulated. A constant pressure of 1 MPa is applied to the upper surface, and the outer surface is fully clamped. The mechanical properties are: $E = 210$ GPa, $\nu = 0.3$. Six successively refined hexahedral meshes are used, with cell counts of 45, 472 (Figure 6), 4 140, 34 968, 287 280 and 2 438 242.

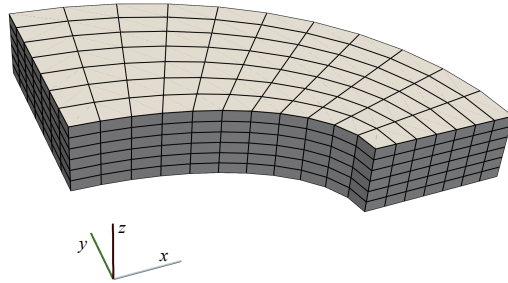


Fig. 6 Elliptic Plate geometry and mesh containing 472 hexahedral cells

The predictions for the equivalent (von Mises) stress along the line $r = \sqrt{x^2 + y^2} = 2.1$ m, $z = 0.3$ m is shown in Figure 7. The results from the finest grid in Demirdžić et al. [17] are given for comparison, where good agreement is seen; the small offset between the finest mesh predictions and those from Demirdžić et al. [17] are likely due to errors introduced when extracting the Demirdžić et al. [17] results using WebPlotDigitizer [19]. The sample values have been calculated by generating 40 uniformly spaced angles between 0 and $\frac{\pi}{2}$ along the line, finding the cell of each sampled point, and extrapolating from the cell-centred value using the field gradient.

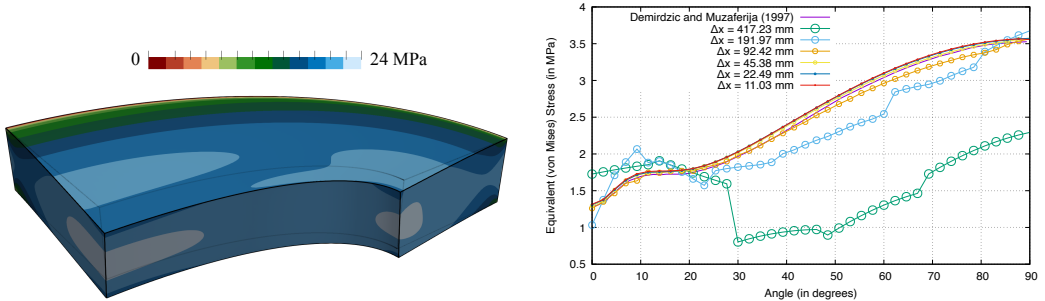


Fig. 7 Equivalent (von Mises) stress distribution in the elliptic plate

Case 3: Narrow T-section component under tension

This case, proposed by Demirdžić et al. [17], consists of a narrow engineering component with a T cross-section (Figure 8). The case is 3-D, static, with linear elastic material behaviour. Symmetry allows one-quarter of the geometry to be simulated. A constant negative pressure of 1 MPa is applied to the lower surface, and the upper left surface is fully clamped. The Young's modulus is $E = 210$ GPa, and Poisson's ratio is $\nu = 0.3$. A radius 5 mm hole is located at the expected stress concentration.

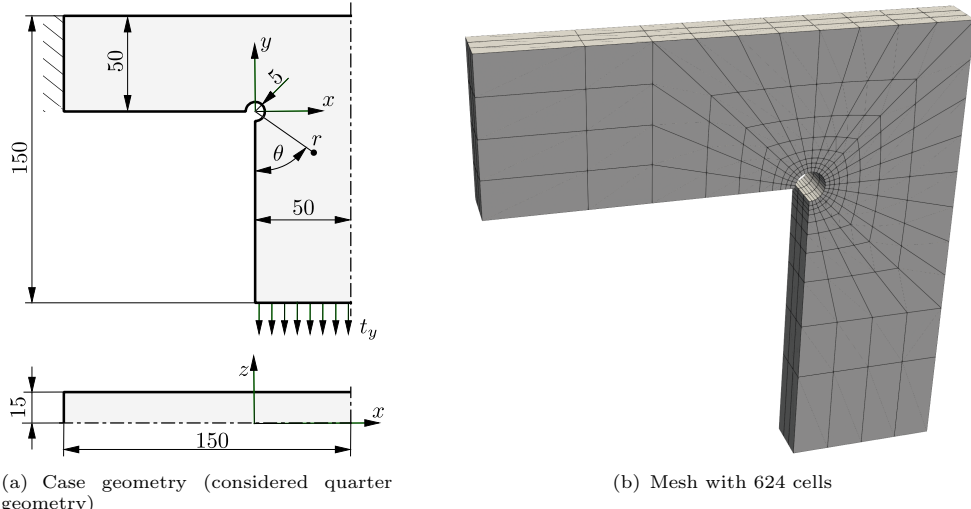
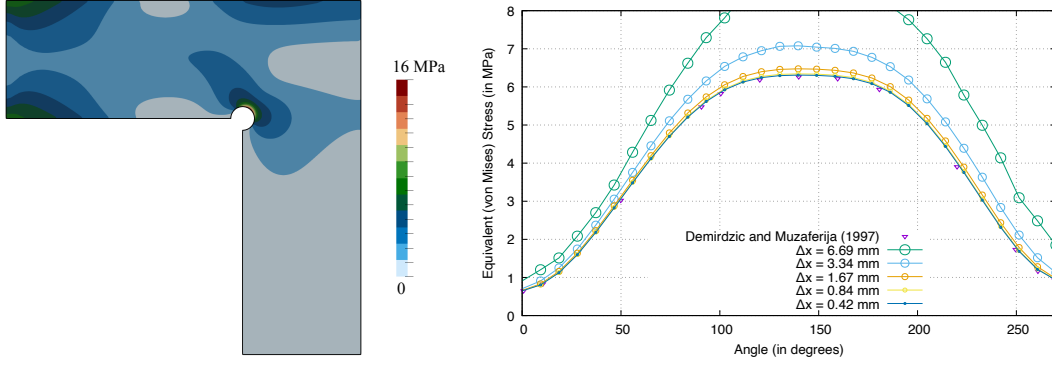


Fig. 8 Narrow T-section component under tension: geometry and mesh

Five successively refined hexahedral meshes are created using the OpenFOAM `blockMesh` utility, consisting of 624, 4 992, 39 936, 319 488, and 2 555 904 cells. The corresponding average cell widths—calculated as the cubed root of the total domain volume divided by the number of cells—are 6.69, 3.34, 1.67, 0.84, and 0.42 mm.

The predicted equivalent (von Mises) stress distribution on the $z = 0$ plane is shown in Figure 9(a), where a stress concentration is apparent near the hole. The equivalent stress along the line $r = 1.5R$, $z = 0$ is shown for the different meshes in Figure 9(b), where R is the hole radius.

The predictions are seen converge to the results reported in Demirdžić et al. [17]. Similarly to the elliptic plate case, the sample values have been to by generating 30 uniformly spaced angles between $-\frac{\pi}{2}$ and $-\pi$ along the line, finding the cell of each sampled point, and extrapolating from the cell-centred value using the field gradient.



(a) Equivalent stress distribution for the mesh with 2555 904 cells on the $z = 0$ m plane

(b) Equivalent stress along the line $r = 1.5R$, $z = 0$ m

Fig. 9 Equivalent (von Mises) stress distribution in the narrow T-section component under tension

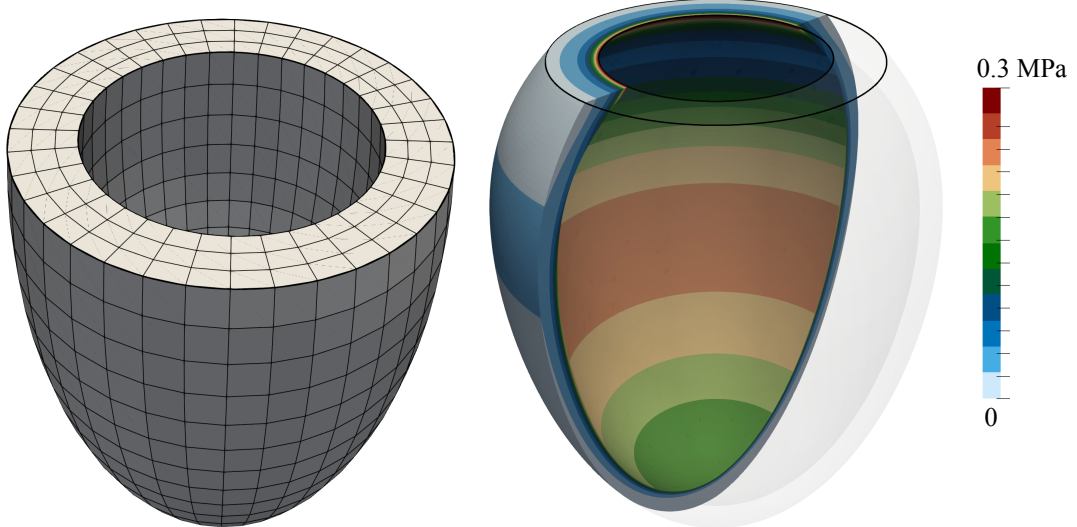
Case 4: Inflation of an idealised ventricle

Inflation of an idealised ventricle (Figure 10) was proposed by Land et al. [20] as a benchmark problem for cardiac mechanics software. The case is 3-D, static, with finite hyperelastic strains. The initial geometry is defined as a truncated ellipsoid:

$$x = r_s \sin(u) \cos(v), \quad y = r_s \sin(u) \sin(v), \quad z = r_l \cos(u) \quad (30)$$

where on the inner (endocardial) surface $r_s = 7$ mm, $r_l = 17$ mm, $u \in [-\pi, -\arccos(\frac{5}{17})]$ and $v \in [-\pi, \pi]$, while on the outer (epicardial) surface $r_s = 10$ mm, $r_l = 20$ mm, $u \in [-\pi, -\arccos(\frac{5}{20})]$ and $v \in [-\pi, \pi]$. The base plane $z = 5$ mm is implicitly defined by the ranges for u . The hyperelastic material behaviour is described by the transversely isotropic constitutive proposed by Guccione et al. [21] law, where the parameters are $C = 10$ kPa, $b_f = b_t = b_{fs} = 1$. The benchmark specifies an incompressible material; in the current work, incompressibility is enforced weakly using a penalty approach, where the bulk modulus parameter is chosen to be two orders of magnitude greater ($\kappa = 1000$ kPa) than the greatest shear modulus parameter. The chosen parameters produce isotropic behaviour. A pressure of 10 kPa is applied to the inner surface, and the base plane is fixed. The geometry is meshed using a structured approach and is predominantly composed of hexahedra, with prism cells forming the apex. The OpenFOAM utilities `blockMesh` and `extrudeMesh` are used to create the meshes. Four successively refined meshes are examined: 1 620 (shown in Figure 10(a)), 12 960, 103 680, and 829 440 cells. The case can be simulated as 2-D axisymmetric but is simulated here using the full 3-D geometry.

The equivalent (von Mises) stress at full inflation is shown for the mesh with 829,440 cells in Figure 10(b), where the high stresses on the endocardial (inner) surface quickly drop off through the wall thickness towards the epicardial (outer) surface. The predicted deformed configuration



(a) Ventricle undeformed geometry, showing the mesh with 1,620 cells
(b) Cross-section showing the equivalent (von Mises) stress distribution for the mesh with 829,440 cells

Fig. 10 Idealised ventricle case

of the midline of the ventricle wall is shown in Figure 11, where a side-by-side comparison is given with the round-robin benchmark results from Land et al. [20]. The predictions are seen to become quickly mesh-independent and fall within the benchmark ranges.

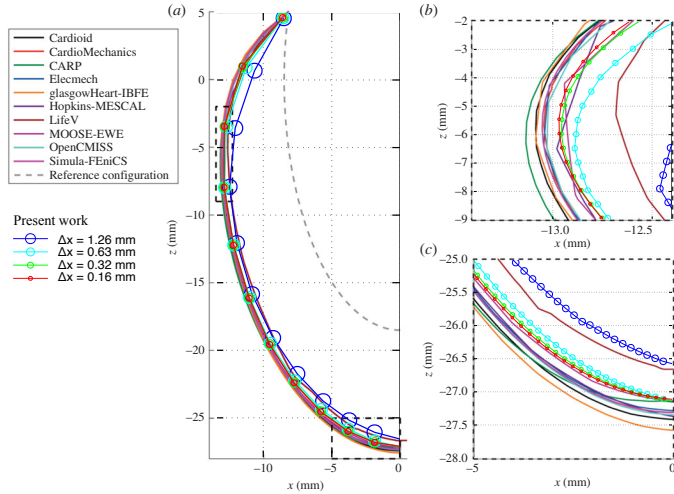


Fig. 11 Idealised ventricle: predictions for the four meshes from the present work overlaid on the round-robin predictions from Land et al. [20]

Case 5: Cook's membrane

Cook's membrane (Figure 12) is a well-known bending-dominated benchmark case used in linear and non-linear analysis. The 2-D plane strain tapered panel (trapezoid) is fixed on one side and subjected to uniform shear traction on the opposite side. The vertices of the trapezoid (in mm) are (0, 0), (48, 44), (48, 60), and (0, 44). The problem is solved quasi-statically, using 30 equally-sized loading increments, and there are no body forces.

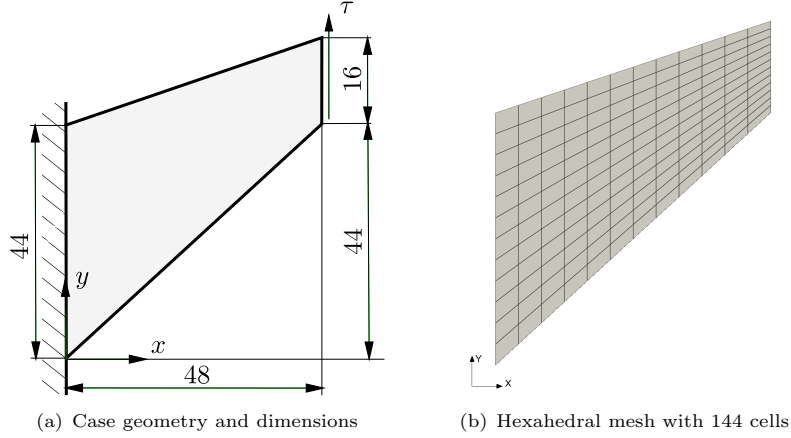


Fig. 12 Cook's membrane case geometry and mesh

The current work considers three forms of the problem:

- i. Small strain linear elastic [22, 23]: $E = 70$ MPa, $\nu = 1/3$, and $\tau = 6250$ Pa.
- ii. Finite strain neo-Hookean hyperelastic [24]: $E = 1.0985$ MPa, $\nu = 0.3$, and $\tau = 0.0625$ MPa.
- iii. Finite strain elastoplastic [23, 25, 26]: $E = 206.9$ MPa, $\nu = 0.29$, $\sigma_y = 0.45 + 0.12924\bar{\varepsilon}_p + (0.715 - 0.45)(1 - e^{-16.93\bar{\varepsilon}_p})$ MPa, and $\tau = 0.3125$ MPa.

where E is the Young's modulus, ν is the Poisson's ratio, σ_y is the yield strength, $\bar{\varepsilon}_p$ is the equivalent plastic strain, and τ is the prescribed shear traction. Seven successively refined quadrilateral meshes are considered, where the cell counts are 9, 36, 144 (Figure 12(b)), 576, 2 304, 9 216, and 36 864.

Figure 13 shows the predicted equivalent stress distribution on the mesh with 36 842 cells for linear elastic, hyperelastic and hyperelastoplastic cases. The stress distribution is consistent with bending, with regions of high stress near the upper and lower surfaces and a line of relatively unstressed material in the centre. The greatest equivalent stresses occur at the top-left corner and the lower surface. In the hyperelastoplastic case, almost the entire domain is plastically yielding with only a small thin region remaining elastic, indicated by the blue line in Figure 13(c).

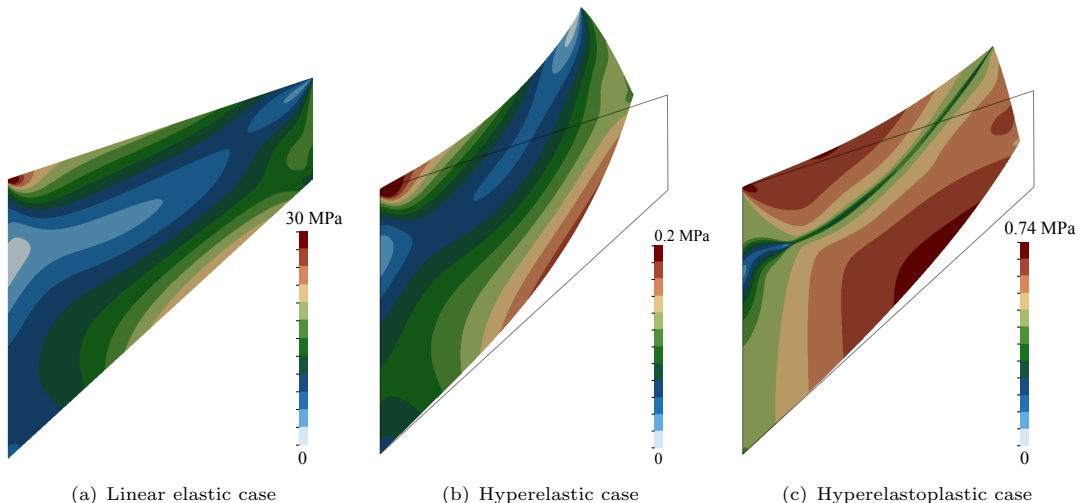


Fig. 13 Equivalent (von Mises) stress distribution for the three Cook's membrane cases using the mesh with 36 842 cells

Figure 14 compares the predicted vertical displacement at the reference point as a function of the average cell widths with results from the literature. The reference point is taken as the top right point – (48,60) mm – in the elastic and hyperelastoplastic cases, while it is taken as the midway point of the loading surface – (48,52) mm – in the hyperelastic case.

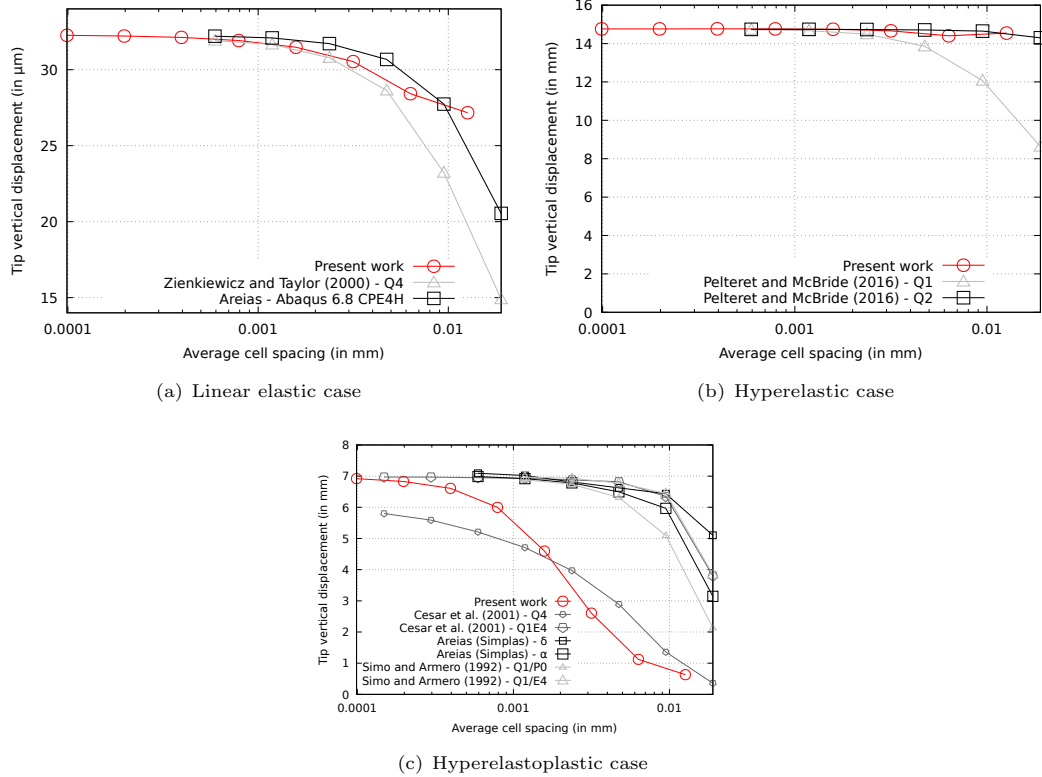


Fig. 14 Cook's membrane vertical displacement predictions at the reference point as a function of the average cell width. Comparisons are given with the results from [22–25].

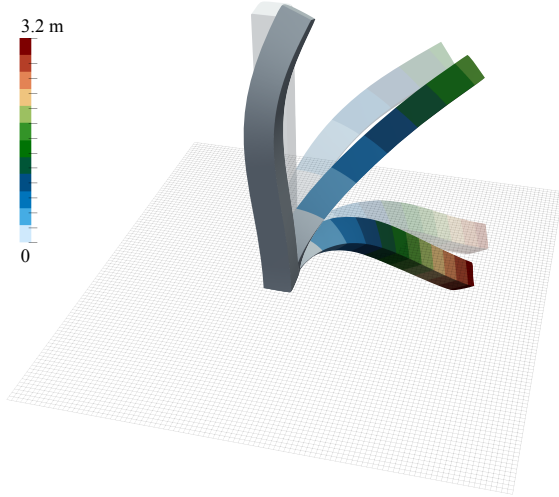
No difference is seen in the predictions whether using the Jacobian-free Newton-Krylov or segregated approach, assuming convergence is achieved. This is expected since both use the same discretisation, and the solution tolerances are shown to ensure the iteration errors are small. Consequently, only the Jacobian-free Newton-Krylov results are shown for the linear elastic and hyperelastic cases. However, the Jacobian-free Newton-Krylov showed poor convergence in the hyperelastoplastic case and failed to converge on many of the meshes. As a result, the results for the segregated approach are presented instead for the hyperelastoplastic case. Discussion of the relative convergence and robustness of the Jacobian-free Newton-Krylov and segregated methods is left to Section 4.2.

Case 6: Vibration of a 3-D Cantilevered Beam

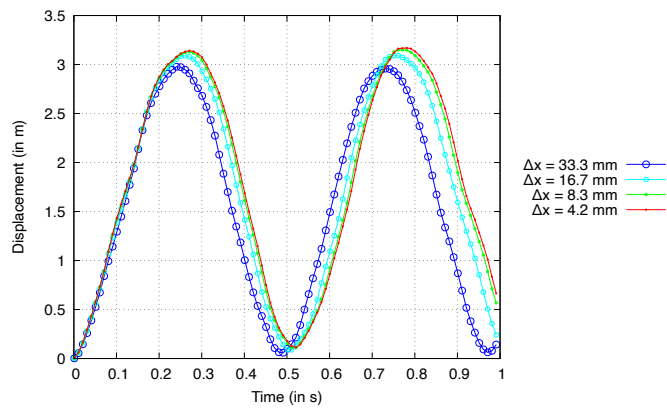
This 3-D, dynamic, finite strain case geometry consists of a $2 \times 0.2 \times 0.2$ m cuboid column and was proposed in its initial form by Tuković and Jasak [27]. A sudden, constant traction $\mathbf{T} = (0.1, 0.1, 0)$ MPa is applied to the upper surface. A neo-Hookean hyperelastic material is assumed with $E = 15.293$ MPa, $\nu = 0.3$ and density $\rho = 1000$ kg m $^{-3}$, while the area $A = 0.04$ m 2 and the second

moment of area $I = \frac{1}{7500} \text{ m}^4$. The geometric and material parameters were chosen for the first natural frequency to be 1 Hz in the small strain limit. The magnitude of the applied traction was chosen to ensure significant geometric nonlinearity, with the upper surface of the beam expected to drop below the plane of the lower surface. Four successively refined hexahedral meshes are generated using the OpenFOAM `blockMesh` utility, with cell counts of 270, 2160, 17280 and 138240. The time step size is 1 ms, and the total period is 10 s.

The deformed configuration of the beam at six time steps is shown in Figure 15(a) for the mesh with 2160 cells, where the upper surface is seen to drop below the horizontal from approximately $t = 0.2$ s to 0.32 s. The corresponding displacement magnitude of the centre of the upper surface of the beam vs time is shown in Figure 15(b).



(a) Displacement magnitude for $t = \{0, 0.1, 0.2\}$ s (translucent) and $t = \{0.3, 0.4, 0.5\}$ s (opaque) for the mesh with 138240 cells



(b) Displacement magnitude of the centre of the upper surface of the beam vs time

Fig. 15 Deflection of a 3-D Cantilevered Beam

Case 7: Axial Turbine Blade

This 3-D, quasi-static, small strain, linear elastic case consists of a twisted axial turbine blade (Figure 16) with the Cartesian axis-aligned bounding box $105.55 \times 177.628 \times 336.5$ mm. This case demonstrates the application of the proposed approach to an industrially-relevant geometry. The blade is constrained at the rotation axis end and subjected to a centrifugal body force $\mathbf{f}_b = \rho\omega^2\mathbf{r}$ kg m $^{-2}$ s $^{-2}$. The scalar rotational velocity $\omega = \frac{2\pi\text{RPM}}{60}$ is defined here about the x axis, where RPM = 720. The vector \mathbf{r} is defined as the shortest vector to the rotation (x) axis. The blade's root is constrained, while all other surfaces are traction-free. A linear elastic material is assumed with $E = 4.431$ GPa, $\nu = 0.33$, and $\rho = 1200$ kg m $^{-3}$. An unstructured polyhedral mesh with 322 161 cells is employed (Figure 16), created in Ansys Fluent and converted to the OpenFOAM format using the `fluent3DMeshToFoam` OpenFOAM utility. Could we include a finer mesh?

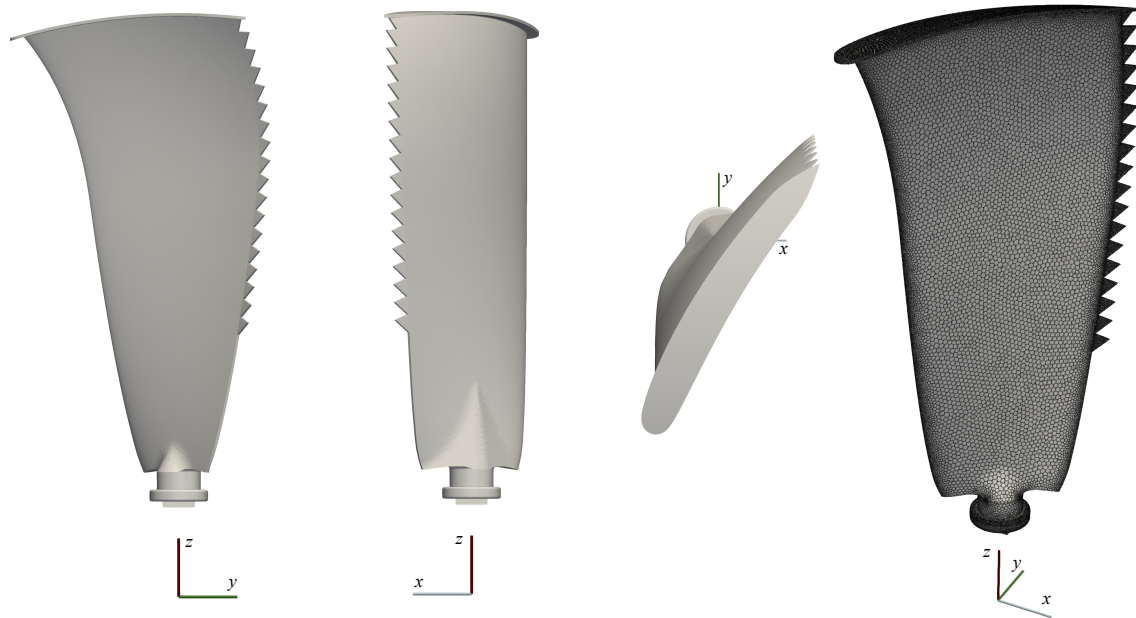


Fig. 16 Axial turbine blade case geometry

The prediction displacement magnitude distribution (left image in Figure 17) is consistent with a cantilever with the largest deflection occurring at the distal free-end of the turbine. The equivalent (von Mises) stress distribution (right image in Figure 17) shows the peak stresses to occur near the blade root and leading and trailing edges, with concentrations near the trailing edge vortex generators **correct name?**.

Case 8: Elastic plate behind a rigid cylinder

Turek and Hron [28] proposed this well-known fluid-solid interaction benchmark case as an extension of the classic flow around a cylinder in a channel problem [29]. The FSI3 variant of the case examined here (Figure 18) consists of a horizontal channel (0.41 m in height, 2.5 m in length) with a rigid cylinder of radius 0.05 m, where the cylinder centre is 0.2 m from the bottom and inlet (left)

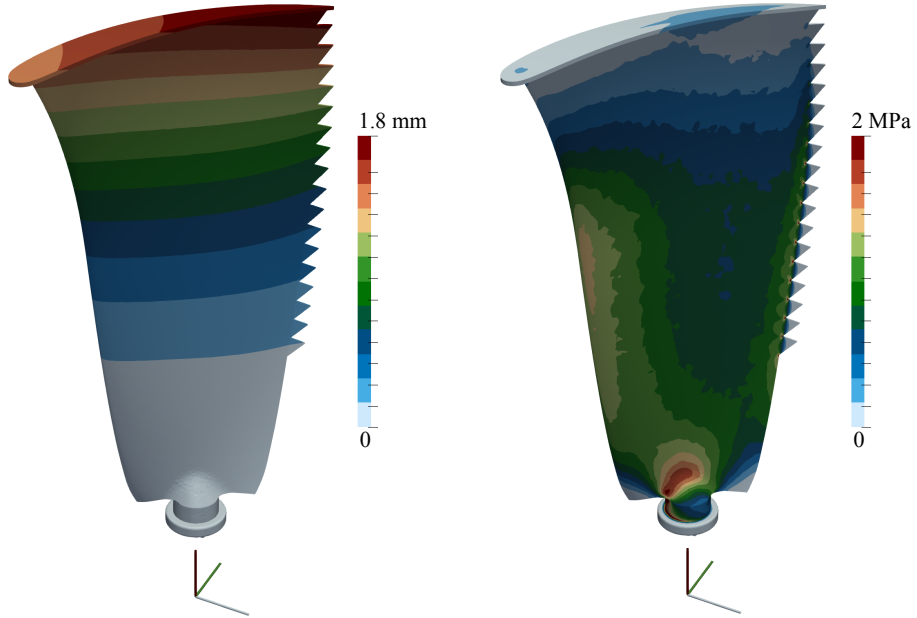


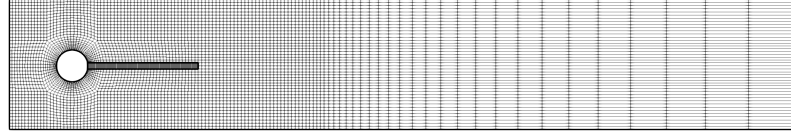
Fig. 17 Axial turbine blade displacement magnitude and equivalent stress distributions [non-smooth stress contours =*i*, indicative of low order of accuracy]

boundaries. A parabolic velocity is prescribed at the inlet velocity with a mean value of 2 m/s. A St. Venant-Kirchhoff hyperelastic plate ($E = 5.6 \text{ MPa}$, $\nu = 0.4$) of 0.35 m in length and 0.02 m in height is attached to the right-hand side of the rigid cylinder. The fluid model is assumed to be isothermal, incompressible, and laminar and adopts the segregated PIMPLE solution algorithm. The fluid's kinematic viscosity is $0.001 \text{ m}^2/\text{s}$ and density is 1000 kg/m^3 , while the solid's density is $10\,000 \text{ kg/m}^3$. The interface- quasi-Newton with inverse Jacobian from a least-squares model coupling approach [30] is employed for the fluid-solid interaction coupling. The fluid-solid interface residual is reduced by four orders of magnitude within each time step. Further details of the fluid-solid interaction procedure are found in Tuković et al. [31]. Three successively refined quadrilateral meshes are employed: The fluid region meshes have 1 252, 5 008, and 20 032 cells, while the solid region meshes have 156, 624 and 2 496 cells. The total simulation time is 20 s, and the time-step size is 0.5 ms.

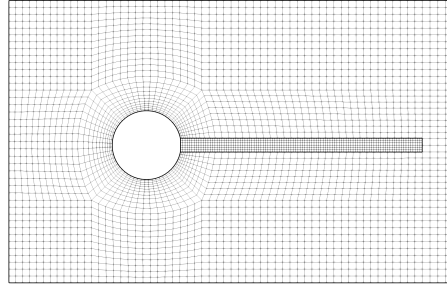
Figure 19 shows the velocity field in the fluid region and displacement magnitude in the solid region at $t = 4.42 \text{ s}$, corresponding to a peak in the vertical displacement of the plate free-end oscillation. The fluid is seen to accelerate as it passes the cylinder, with regular vortices being thrown off the plate, causing it to oscillate. The predicted mean, amplitude and frequency of the vertical and horizontal displacement of the end of the plate are compared with the results from Turek and Hron [28] in Table 1. As directed in Turek and Hron [28], the maximum and minimum values for the last period are used to calculate the mean and amplitude:

$$\text{mean} = \frac{1}{2}(\max + \min), \quad \text{amplitude} = \frac{1}{2}(\max - \min) \quad (31)$$

while the frequency is calculated as the inverse of the period.



(a) Mesh containing 5 336 cells in the fluid region and 630 cells in the solid region, where a closeup of the plate is shown in the right



(b) Close-up of the mesh around the plate

Fig. 18 Elastic plate behind a rigid cylinder case geometry and mesh

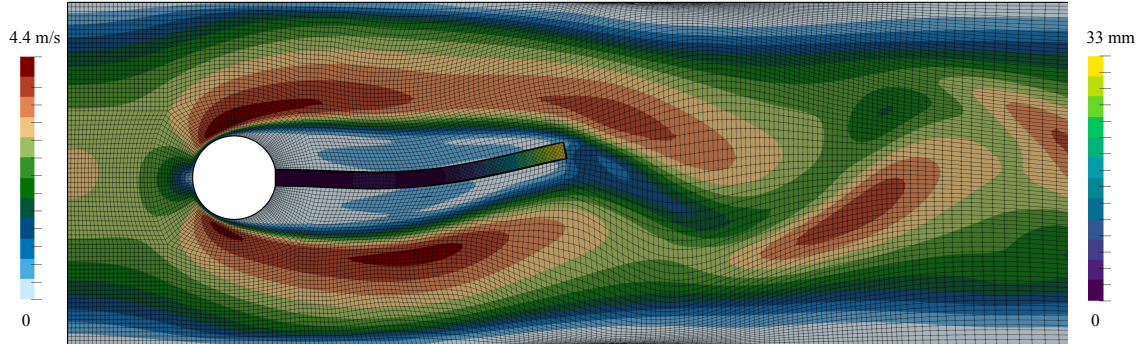


Fig. 19 Elastic plate behind a rigid cylinder case results at $t = 20$ s for the mesh with 20 032 cells in the fluid region and 2 496 in the solid region. The velocity magnitude is shown in the fluid region while the displacement magnitude is shown in the solid region.

Mesh (number of fluid and solid cells)	u_x (in mm)	u_y (in mm)
1 (1 252 + 156)	-0.1 ± 0.001 [47.6]	1.58 ± 0.002 [5.88]
2 (5 008 + 624)	-2.16 ± 2.00 [10.2]	1.54 ± 29.56 [5.6]
3 (20 032 + 2 496)	-2.51 ± 2.37 [12.1]	0.87 ± 33.08 [5.6]
Turek and Hron [28]	-2.69 ± 2.53 [10.9]	1.48 ± 34.38 [5.3]

Table 1 Average predicted displacements (mean \pm amplitude [frequency]) of the free end of the plate. Note that large-scale plate oscillations in mesh 1 (coarsest mesh) die out within the first 10 s.

4.2 Resource Requirements and Robustness

This section compares resource requirements and robustness of the Jacobian-free Newton-Krylov and segregated approaches on the cases presented in Section 4.1. Specifically, time and memory requirements are analysed, and cases where either approach diverges are examined. In some cases, time and memory requirements from finite element software **Abaqus** are given for reference. In all cases, the Jacobian-free Newton-Krylov approach used the generalised minimal residual method (GMRES) linear solver with the direct LU preconditioner for 2-D and the Hypre *BoomerAMG* multigrid preconditioner for 3-D. In contrast, The segregated approach used the conjugate gradient

linear solver and the Hypre *BoomerAMG* multigrid preconditioner for all cases. Time and memory requirements are implementation and hardware-specific; nonetheless, it is insightful to see the relative performances of the Jacobian-free Newton-Krylov and segregated approaches on the same hardware and within the same implementation framework. Clock times and memory usage (measured with the GNU time utility) were generated using a Mac Studio with an M2 Ultra CPU on one CPU core, where the code was built with the Clang compiler. Examination of multi-CPU-core parallelisation is left to Section 4.5.

Table 2 lists the wall clock times (time according to a clock on the wall) and maximum memory usage for all cases and all meshes. Figure 21(a) plots the corresponding speedup on all cases as a function of the number of degrees of freedom, where the speedup is defined as the segregated clock time divided by the Jacobian-free Newton-Krylov clock time. The number of degrees of freedom is $2 \times$ the cell count in 2-D cases and $3 \times$ in 3-D cases, except in the fluid-solid interaction case where the fluid domain has three degrees of freedom (two velocity components and pressure) in 2-D. Speedup is only calculated for clock times greater than 2 seconds to avoid the comparison of small numbers. In all cases where convergence was achieved, the Jacobian-free Newton-Krylov approach was faster (speedup > 1), with speedups of one or two orders of magnitude in many cases. Additionally, it can be observed from Figure 21(a) that the speedup increases as the number of degrees of freedom increases. The largest speedup was 237 on the finest mesh of the membrane i (2-D, linear elastic) case, while the lowest speed was 1.09 and occurred on the coarsest mesh in the fluid-solid interaction case. Excluding the fluid-solid interaction, where the majority of degrees of freedom are placed in the fluid region, the next lowest speed-up was 1.66 and occurred on a coarse mesh in the membrane ii (2-D, hyperelastic) case.

Figure 20(b) shows the *relative memory* usage, defined here as the maximum memory usage of the segregated approach divided by that of the Jacobian-free Newton-Krylov approach. The relative memory usage is close to unity in most cases, indicating there is no significant increase in memory requirements when switching from a segregated approach to a Jacobian-free Newton-Krylov approach. In addition, unlike for the speedup, there is no general trend in the relative memory usage as the number of degrees of freedom increases. The maximum value for relative memory was 1.9 and occurred in the second-finest mesh for the membrane ii (2-D, hyperelastic) case, although for all other meshes in this case, the value was less than one (between 0.82 and 0.95). The maximum memory usage is primarily attributed to the linear solver and preconditioner; the choice of preconditioner and linear solver settings are examined further in Section 4.3.

Note: we use segregated in PETSc, so it is a vector system

Regarding robustness, the Jacobian-free Newton-Krylov approach converged in all cases bar one, requiring less than five outer Newton iterations on average in all converged cases. The only case where the Jacobian-free Newton-Krylov approach failed to converge was for the Membrane iii problem, the only elastoplastic case examined. For the failed meshes, they each reached approximately 80% of the total load before the linear solver diverged. The cause of this divergence is likely related to the proposed compact preconditioner matrix, which is formulated based on small *elastic* strains, being a poor approximation of the true Jacobian for large plastic strains. Interestingly, convergence problems were not encountered in the hyperelastic cases (Membrane ii, Ventricle, Cantilever, Fluid-solid interaction), demonstrating that the proposed compact *linear elastic* preconditioner matrix is suitable for such large strain hyperelastic cases. In contrast, the segregated

Case	Cell Count	JFNK		Segregated	
		Time (in s)	Memory (in MB)	Time (in s)	Memory (in MB)
MMS <i>3-D, static, linear elastic</i>	384	0	78	0	79
	4 374	0	86	0	94
	41 154	1	195	2	181
	355 914	4	1 063	9	1 289
	2 958 234	41	6 724	92	6 174
	24 118 074	486	30 606	1 732	30 601
Elliptic Plate <i>3-D, static, linear elastic</i>	45	0	72	0	76
	472	0	78	0	81
	4 140	1	153	8	124
	34 968	7	754	149	660
	287 280	95	3 943	2 694	3 661
	2 438 242	988	21 884	45 692	20 348
T-member <i>3-D, static, linear elastic</i>	624	0	84	1	85
	4 992	1	127	7	141
	39 936	10	557	133	723
	319 488	154	4 024	2 916	3 547
	2 555 904	1 751	22 814	47 344	21 827
	1 620	54	133	†	†
Ventricle <i>3-D, static, hyperelastic</i>	12 960	576	553	†	†
	103 680	8 362	3 435	†	†
	829 440	150 023	11 746	†	†
	9	0	77	0	76
Membrane i <i>2-D, static, linear elastic</i>	36	0	77	0	76
	144	0	78	0	78
	576	0	82	1	84
	2 304	0	94	4	102
	9 216	1	152	33	186
	36 864	2	497	444	392
	147 456	10	1 461	2 371	1 950
	9	1	81	1	78
	36	1	81	2	78
	144	3	84	5	80
Membrane ii <i>2-D, static, hyperelastic</i>	576	9	97	26	91
	2 304	34	144	166	132
	9 216	161	256	1 374	357
	36 864	860	554	15 991	1 053
	147 456	1 585	2 847	135 851	2 341
	9	0	78	3	78
	36	1	79	6	79
Membrane iii <i>2-D, static, hyperelastoplastic</i>	144	†	†	27	82
	576	8	90	231	104
	2 304	†	†	1 379	180
	9 216	†	†	8 321	451
	36 864	†	†	60 698	1 396
	147 456	†	†	341 212	3 466
	270	11	85	†	†
Cantilever <i>3-D, dynamic, hyperelastic</i>	2 160	71	181	†	†
	17 280	854	752	†	†
	138 240	11 800	5 790	†	†
	322 161	22 782	11 102		rnnng
Turbine <i>3-D, static, linear elastic</i>	2 493 299	to-rn			to-rn
	1 252 + 156	3 830	748	5 360	738
	5 008 + 624	32 074	834	52 372	775
FSI <i>2-D, dynamic, hyperelastic</i>	20 032 + 2 496	170 919	785	218 797	748

Table 2 Execution times (rounded to the nearest second) and maximum memory usage for Jacobian-free Newton-Krylov (JFNK) and segregated methods (rounded to the nearest MB). † indicates the solver crashed.

approach—which uses the same matrix—had no problems with the elastoplastic case (Membrane iii) but failed to converge on two of the hyperelastic cases (Ventricle, Cantilever). In both cases where the segregated approach failed, large elastic strains and large rotations were observed, and the segregated solver failed in the early time steps. It is interesting to note that the same linear elastic preconditioner matrix works well with the Jacobian-free Newton-Krylov approach for

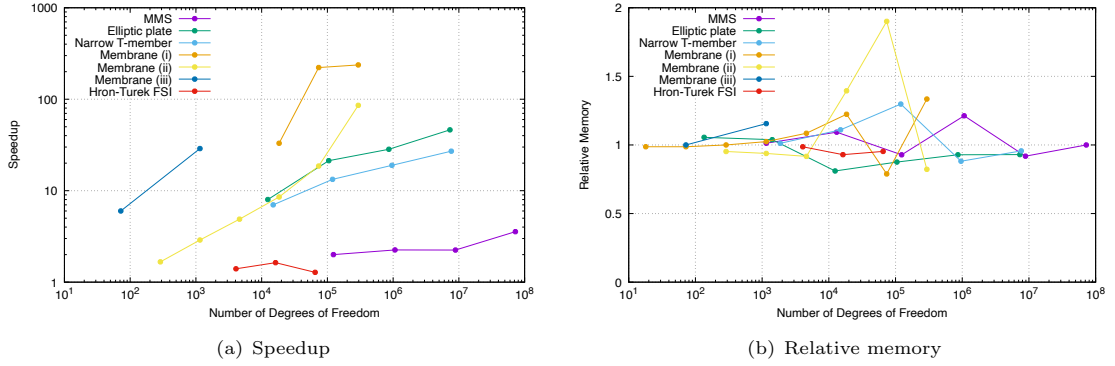


Fig. 20 The speedup (segregated clock time divided by the Jacobian-free Newton-Krylov clock time) and relative memory usage (segregated maximum memory usage divided by the Jacobian-free Newton-Krylov maximum memory usage) as a function of degrees of freedom

hyperelastic cases but not for the segregated approach, while the opposite is true for elastoplastic cases.

Regarding geometric dimension, the same general trends are observed in 2-D and 3-D, with no major distinctions in behaviour. The same can be said for geometric nonlinearity (small strain vs. large strain) with similar speed-ups for both linear elastic and hyperelastic cases. One observation worth highlighting is the relatively lower speed for the method of manufactured solutions case (3-D, linear elastic): a possible explanation is that the segregated approach has previously been seen to be efficient on geometry with low aspect ratios (ratio of maximum to minimum dimensions); in this case, the aspect ratio is at its minimum (unity). In contrast, in other 3-D, linear elastic cases (Elliptic plate, Narrow T-Member, Membrane i, Turbine), the aspect ratios are greater than unity, and the segregated approach performs worse relative to the Jacobian-free Newton-Krylov approach.

Should we add Table 1 for other hardware in the appendix?

4.3 Effect of the Preconditioner Choice

This section examines the effect of preconditioning procedure choice on the performance of the Jacobian-free Newton Krylov approach. Three choices of preconditioning procedure are compared:

- **LU** - The *MUltifrontal Massively Parallel sparse direct Solver* (MUMPS) [32, 33] LU decomposition direct solver. A direct solver is expected to be the more robust but may suffer from excessive time and memory requirements for larger numbers of unknowns.
- **ILU(N)** - Incomplete LU decomposition with N fill-in. ILU(N) is expected to have lower memory requirements than the LU direct solver but at the expense of robustness. As the system of unknowns becomes larger, the number of ILU(N) iterations is expected to increase. As the fill-in factor N increases, ILU(N) approaches the behaviour of a LU direct solver.
- **Algebraic multigrid** - The Hypre Boomerang [34] parallelised multigrid preconditioner. Multigrid approaches have the potential to offer superior performance than other methods for larger problems, with near linear scaling of time and memory requirements.

An additional consideration when selecting a preconditioner is its ability to scale in parallel as the number of CPU cores increases. From this perspective, the iterative approaches (ILU(N) and multigrid) are expected to show better parallel scaling than direct methods (LU). Analysis of this point is left to Section 4.5.

The preconditioning approaches are compared in three cases: membrane i (2-D, linear elastic), elliptic plate (3-D, linear elastic), and idealised ventricle (3-D, hyperelastic).

Figure 21 compares the clock times and maximum memory requirements for the three preconditioning approaches as a function of degrees of freedom. ILU1 diverges on the ventricle for the finer two meshes: re-rnng with ILU2 LU ventricle: mesh4 is running Comment on the results: e.g. fastest, slowest, most/least iterations, etc Provide insights, if any: e.g. why is one faster or slower Conclusion: which preconditioner is 'best' for which situation: probably LU is best for 'small' cases and multigrid for 'large' cases

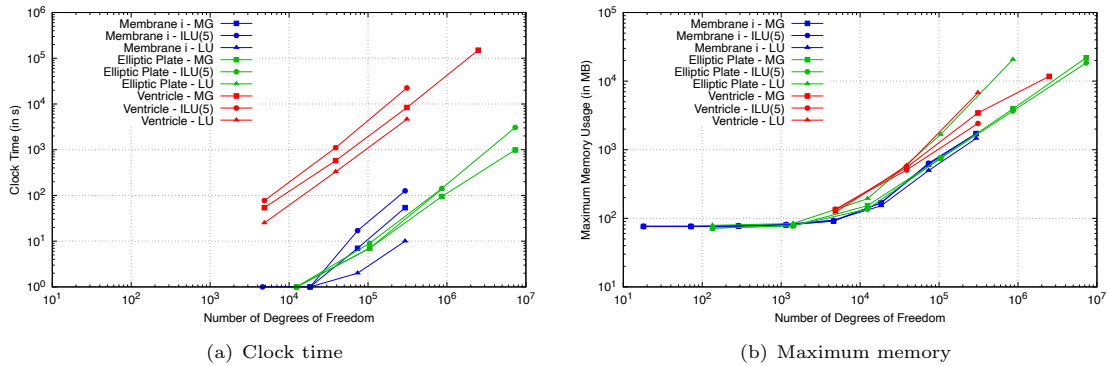


Fig. 21 The clock times and maximum memory usage for three preconditioning approaches (multigrid, ILU(1), and LU) as a function of degrees of freedom

Other linear solver settings: mention these but no need for analyses

In GMRES, we must choose the value of the "restarts" parameter; the default in PETSc of 30 does not always seem good enough (I have been setting it to 100). We could show its affect on one case. I think the optimal choice is linked with the choice of preconditioner (a better preconditioner means we can use a small restart value) so maybe we include this with the "preconditioner choices" section. I suggest we do not add an analysis of this: instead we can just mention it

This can also be considered a linear solver setting. For segregated, we always use a relative tolerance of 0.1, but initial tests for JFNK show that 0.1 is too loose and 1e-3 seems better, although maybe there is no difference with using 1e-6. I suggest we do not add an analysis of this: instead we can just mention it

4.4 Effect of Rhie-Chow Stabilisation

This section highlights the effect of the choice of the global scaling factor α in the Rhie-Chow stabilisation (Equation 17) on the performance of the proposed Jacobian-free Newton Krylov method.

As described in Section 2.3, the stabilisation term is introduced to quell zero-energy modes (oscillations) in the discrete solution, such as checkerboarding. As the amount of stabilisation increases (increasing α), these numerical modes are quelled, and the solution stabilises; however, at some point, further increases in the amount of stabilisation reduce the accuracy of the discretisation due to over-smoothing. A less obvious consequence of changing the stabilisation magnitude is its effect on the convergence of the linear solver in the Jacobian-free Newton-Krylov solution procedure. This section examines this effect. Similar analyses have been performed by, for example, [?] for a **XXX** Euler flow finite volume formulation using a Jacobian-free Newton-Krylov approach.

As in the previous section, three cases are used to highlight the effect: membrane i (2-D, linear elastic), elliptic plate (3-D, linear elastic), and idealised ventricle (3-D, hyperelastic). The LU preconditioning method is used for the 2-D membrane i case, while the multigrid approach is used for the two 3-D cases. Figure 22 presents the execution times and the number of accumulated linear solver iterations for three values of global stabilisation factor ($\alpha = [0.01, 0.1, 1]$) for several mesh densities. The memory usage is unaffected by the value of α and is hence not shown.

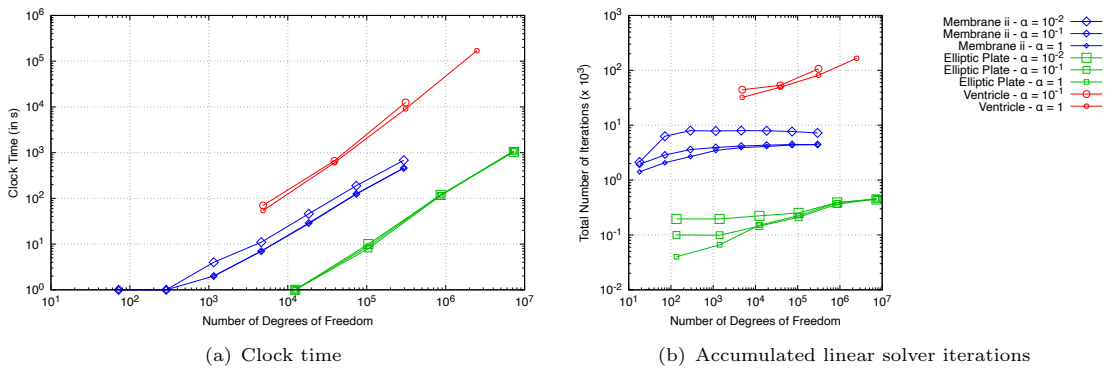


Fig. 22 The clock times and accumulated linear solver iterations for different values of Rhee-Chow global stabilisation factor α

Figure 23 shows a comparison of the stress (or displacement) along the line **XXX** - ; we need to show the effect on accuracy for different values of alpha

placeholder

Fig. 23 Stress predictions along the line **XXX** for the **YYY** case using different values of the Rhee-Chow stabilisation factor α

4.5 Parallelisation

In this final analysis, the multi-CPU-core parallel scaling performance of the proposed Jacobian-free Newton Krylov method is examined. Two types of parallel scaling analyses are performed [5]:

- Strong scaling study: Strong scaling measures how the execution time of a fixed problem size (fixed number of cells) decreases as the number of CPU cores increases. Good strong scaling indicates that an application effectively utilises additional CPU cores without significant overhead. In contrast, poor strong scaling suggests that adding more cores does not significantly reduce the execution time, often due to increased communication or synchronisation overhead.
- Weak scaling study: Weak scaling measures how the execution time changes as the problem size (the number of cells) and the number of CPU cores increase proportionally, where the problem size per CPU core remains (approximately) constant. Good weak scaling indicates that the application can efficiently manage larger workloads with more cores without a significant increase in execution time. Poor weak scaling implies that the application struggles to maintain performance as the problem size and core count increase.

The results from the strong scaling study are shown in Figure 24. The speedup S is defined as $S = t_1/t_p$, where t_1 is the clock time on one CPU core and t_p is the clock time on P CPU cores. In the ideal case, the speedup should double when the number of cores is doubled. In reality, inter-CPU-core communication reduces the parallel scaling efficiency below the ideal. Comment on the results: e.g. fastest, slowest, most/least iterations, best/worst scaling. Provide insights, if any: e.g. why is one faster or slower

placeholder placeholder

(a) Clock times vs number of CPU cores (b) Speedup S vs number of CPU cores

Fig. 24 Strong parallel scaling study comparing the performance of three preconditioning strategies: a LU direct solver, and ILU(N) and multigrid iterative solvers

The weak scaling results are shown in Figure 25. The weak scaling efficiency η_w is defined as $\eta_w = t^{[w]}_1/t^{[w]}_p$, where $t^{[w]}_1$ is the clock time on one CPU core and $t^{[w]}_p$ is the clock time on P CPU cores where the problem size per CPU core is constant. In the ideal case, the efficiency should be unity, but inter-CPU-core communication reduces it. Comment on the results: e.g. fastest, slowest, most/least iterations, best/worst scaling. Provide insights, if any: e.g. why is one faster or slower

Compare preconditioners

(a) Clock times vs number of CPU cores
(b) Weak scaling efficiency η_w vs number of CPU cores

Fig. 25 Weak parallel scaling study comparing the performance of three preconditioning strategies: a LU direct solver, and ILU(N) and multigrid iterative solvers

5 Conclusions

In the current work, a Jacobian-free Newton-Krylov solution algorithm has been proposed for solid mechanics problems discretised using the cell-centred finite volume method. A compact-stencil discretisation of the diffusion term is proposed as the preconditioner matrix, allowing a straightforward extension of existing segregated solution frameworks. The key findings of the work are:

- Main results
- Main important choices
- How it compares to segregated methods and FE (Abaqus)

Potentially, modifying the compact preconditioner matrix to account for plasticity would allow the method to work in the failed cases, but this will be left for future studies.

Acknowledgments. This project has received funding from the European Research Council (ERC) under the European Union’s Horizon 2020 research and innovation programme (Grant Agreement No. 101088740). Financial support is gratefully acknowledged from the Irish Research Council through the Laureate programme, grant number IRCLA/2017/45, from Bekaert through the University Technology Centre (UTC phases I and II) at UCD (www.ucd.ie/bekaert), from I-Form, funded by Science Foundation Ireland (SFI) Grant Numbers 16/RC/3872 and RC2302_2, co-funded under European Regional Development Fund and by I-Form industry partners, and from NexSys, funded by SFI Grant Number 21/SPP/3756. Additionally, the authors wish to acknowledge the DJEI/DES/SFI/HEA Irish Centre for High-End Computing (ICHEC) for the provision of computational facilities and support (www.ichec.ie), and part of this work has been carried out using the UCD ResearchIT Sonic cluster which was funded by UCD IT Services and the UCD Research Office. **Ivan/Zeljko: add any additional acknowledgements here**

Appendix A Truncation Error Analysis of the Rhie-Chow Stabilisation Term

On a 1-D uniform mesh with spacing Δx and unity areas, the Rhie-Chow term stabilisation term (Equation 17) for centre cell P becomes

$$\begin{aligned}\mathcal{D}_{\text{Rhie-Chow}} &= \sum_{f \in N_f} \alpha \bar{K}_f \left[|\Delta_f| \frac{\mathbf{u}_{N_f} - \mathbf{u}_P}{|\mathbf{d}_f|} - \Delta_f \cdot (\nabla \mathbf{u})_f \right] |\Gamma_f| \\ &= \alpha \bar{K} \left[\frac{\mathbf{u}_E - \mathbf{u}_P}{\Delta x} - (\nabla \mathbf{u})_e \right] + \alpha \bar{K} \left[\frac{\mathbf{u}_W - \mathbf{u}_P}{\Delta x} + (\nabla \mathbf{u})_w \right]\end{aligned}\quad (\text{A1})$$

where E and W indicate the east and west neighbour cell centre values, EE and WW are the far east and west neighbour cell centre values, and e and w indicate east and west face values; α and \bar{K} are assumed uniform. The face gradients are calculated as

$$\begin{aligned}(\nabla \mathbf{u})_e &= \frac{1}{2} [(\nabla \mathbf{u})_P + (\nabla \mathbf{u})_E] \\ (\nabla \mathbf{u})_w &= \frac{1}{2} [(\nabla \mathbf{u})_W + (\nabla \mathbf{u})_P]\end{aligned}\quad (\text{A2})$$

where the cell centre gradients are calculated as

$$\begin{aligned}(\nabla \mathbf{u})_W &= \frac{\mathbf{u}_P - \mathbf{u}_{WW}}{2\Delta x} \\ (\nabla \mathbf{u})_P &= \frac{\mathbf{u}_E - \mathbf{u}_W}{2\Delta x} \\ (\nabla \mathbf{u})_E &= \frac{\mathbf{u}_{EE} - \mathbf{u}_P}{2\Delta x}\end{aligned}\quad (\text{A3})$$

The final Rhie-Chow term becomes

$$\begin{aligned}\mathcal{D}_{\text{Rhie-Chow}} &= \alpha \bar{K} \left\{ \frac{\mathbf{u}_E - \mathbf{u}_P}{\Delta x} - \frac{1}{2} [(\nabla \mathbf{u})_P + (\nabla \mathbf{u})_E] + \frac{\mathbf{u}_W - \mathbf{u}_P}{\Delta x} + \frac{1}{2} [(\nabla \mathbf{u})_W + (\nabla \mathbf{u})_P] \right\} \\ &= \alpha \bar{K} \left\{ \frac{\mathbf{u}_E - \mathbf{u}_P}{\Delta x} - \frac{1}{2} (\nabla \mathbf{u})_E + \frac{\mathbf{u}_W - \mathbf{u}_P}{\Delta x} + \frac{1}{2} (\nabla \mathbf{u})_W \right\} \\ &= \alpha \bar{K} \left[\frac{\mathbf{u}_E - \mathbf{u}_P}{\Delta x} - \frac{\mathbf{u}_{EE} - \mathbf{u}_P}{4\Delta x} + \frac{\mathbf{u}_W - \mathbf{u}_P}{\Delta x} + \frac{\mathbf{u}_P - \mathbf{u}_{WW}}{4\Delta x} \right] \\ &= \frac{\alpha \bar{K}}{4\Delta x} [-\mathbf{u}_{WW} + 4\mathbf{u}_W - 6\mathbf{u}_P + 4\mathbf{u}_E - \mathbf{u}_{EE}]\end{aligned}\quad (\text{A4})$$

A local truncation analysis can be performed using the following truncated Taylor series about the true solution (\mathbf{U}) and its gradients $((\nabla \mathbf{U})_P, (\nabla^2 \mathbf{U})_P, \dots)$ at P :

$$\begin{aligned}\mathbf{u}_{WW} &= \mathbf{U}_P - 2\Delta x (\nabla \mathbf{U})_P + \frac{4\Delta x^2}{2!} (\nabla^2 \mathbf{U})_P - \frac{8\Delta x^3}{3!} (\nabla^3 \mathbf{U})_P + O(\Delta x^4) \\ \mathbf{u}_W &= \mathbf{U}_P - \Delta x (\nabla \mathbf{U})_P + \frac{\Delta x^2}{2!} (\nabla^2 \mathbf{U})_P - \frac{\Delta x^3}{3!} (\nabla^3 \mathbf{U})_P + O(\Delta x^4)\end{aligned}$$

$$\begin{aligned}
\mathbf{u}_P &= \mathbf{U}_P \\
\mathbf{u}_E &= \mathbf{U}_P + \Delta x (\nabla \mathbf{U})_P + \frac{\Delta x^2}{2!} (\nabla^2 \mathbf{U})_P + \frac{\Delta x^3}{3!} (\nabla^3 \mathbf{U})_P + O(\Delta x^4) \\
\mathbf{u}_{EE} &= \mathbf{U}_P + 2\Delta x (\nabla \mathbf{U})_P + \frac{4\Delta x^2}{2!} (\nabla^2 \mathbf{U})_P + \frac{8\Delta x^3}{3!} (\nabla^3 \mathbf{U})_P + O(\Delta x^4)
\end{aligned} \tag{A5}$$

where $O(\Delta x^4)$ are higher-order terms with a leading term proportional to Δx^4 .

Substituting the expressions above (Equations A5) for the true solution into Equation A4 results in

$$\begin{aligned}
\mathcal{D}_{\text{Rhie-Chow}} &= \frac{\alpha \bar{K}}{4\Delta x} [-\mathbf{u}_{WW} + 4\mathbf{u}_W - 6\mathbf{u}_P + 4\mathbf{u}_E - \mathbf{u}_{EE}] \\
&= \frac{\alpha \bar{K}}{4\Delta x} \left[-\mathbf{U}_P + 2\Delta x (\nabla \mathbf{U})_P - 4\frac{\Delta x^2}{2!} (\nabla^2 \mathbf{U})_P + 8\frac{\Delta x^3}{3!} (\nabla^3 \mathbf{U})_P \right. \\
&\quad + 4\mathbf{U}_P - 4\Delta x (\nabla \mathbf{U})_P + 4\frac{\Delta x^2}{2!} (\nabla^2 \mathbf{U})_P - 4\frac{\Delta x^3}{3!} (\nabla^3 \mathbf{U})_P \\
&\quad - 6\mathbf{U}_P \\
&\quad + 4\mathbf{U}_P + 4\Delta x (\nabla \mathbf{U})_P + 4\frac{\Delta x^2}{2!} (\nabla^2 \mathbf{U})_P + 4\frac{\Delta x^3}{3!} (\nabla^3 \mathbf{U})_P \\
&\quad \left. - \mathbf{U}_P - 2\Delta x (\nabla \mathbf{U})_P - 4\frac{\Delta x^2}{2!} (\nabla^2 \mathbf{U})_P + 8\frac{\Delta x^3}{3!} (\nabla^3 \mathbf{U})_P + O(\Delta x^4) \right] \\
&= \frac{\alpha \bar{K}}{4\Delta x} \left[16\frac{\Delta x^3}{3!} (\nabla^3 \mathbf{U})_P + O(\Delta x^4) \right] \\
&= \frac{2}{3}\alpha \bar{K} \Delta x^2 (\nabla^3 \mathbf{U})_P + O(\Delta x^3)
\end{aligned} \tag{A6}$$

The leading truncation error is proportional to Δx^2 ! Did I make a mistake...?

Appendix B Body Force for the Method of Manufactured Solutions Case

The body force for the manufactured solution case is

$$f_b = \begin{cases} \lambda [8a_y\pi^2 \cos(4\pi x) \cos(2\pi y) \sin(\pi z) \\ + 4a_z\pi^2 \cos(4\pi x) \cos(\pi z) \sin(2\pi y) \\ - 16a_x\pi^2 \sin(4\pi x) \sin(2\pi y) \sin(\pi z)] \\ + \mu [8a_y\pi^2 \cos(4\pi x) \cos(2\pi y) \sin(\pi z) \\ + 4a_z\pi^2 \cos(4\pi x) \cos(\pi z) \sin(2\pi y) \\ - 5a_x\pi^2 \sin(4\pi x) \sin(2\pi y) \sin(\pi z)] \\ - 32a_x\mu_\pi^2 \sin(4\pi x) \sin(2\pi y) \sin(\pi z) \\ \\ \lambda [8a_x\pi^2 \cos(4\pi x) \cos(2\pi y) \sin(\pi z) \\ + 2a_z\pi^2 \cos(2\pi y) \cos(\pi z) \sin(4\pi x) \\ - 4a_y\pi^2 \sin(4\pi x) \sin(2\pi y) \sin(\pi z)] \\ + \mu [8a_x\pi^2 \cos(4\pi x) \cos(2\pi y) \sin(\pi z) \\ + 2a_z\pi^2 \cos(2\pi y) \cos(\pi z) \sin(4\pi x) \\ - 17a_y\pi^2 \sin(4\pi x) \sin(2\pi y) \sin(\pi z)] \\ - 8a_y\mu_\pi^2 \sin(4\pi x) \sin(2\pi y) \sin(\pi z) \\ \\ \lambda [4a_x\pi^2 \cos(4\pi x) \cos(\pi z) \sin(2\pi y) \\ + 2a_y\pi^2 \cos(2\pi y) \cos(\pi z) \sin(4\pi x) \\ - a_z\pi^2 \sin(4\pi x) \sin(2\pi y) \sin(\pi z)] \\ + \mu [4a_x\pi^2 \cos(4\pi x) \cos(\pi z) \sin(2\pi y) \\ + 2a_y\pi^2 \cos(2\pi y) \cos(\pi z) \sin(4\pi x) \\ - 20a_z\pi^2 \sin(4\pi x) \sin(2\pi y) \sin(\pi z)] \\ - 2a_z\mu_\pi^2 \sin(4\pi x) \sin(2\pi y) \sin(\pi z) \end{cases} \quad (B7)$$

where μ and λ are the first and second Lamé parameters, respectively.

Appendix C Analytical Expressions for the Stress and Displacement Distributions around a Spherical Cavity under Uniaxial Tensions

The analytical expressions for the stress distributions around the cavity, first derived by Southwell and Gough [35], are

$$\sigma_{rr} = \frac{T}{14 - 10\nu} \frac{a^3}{R^3} \left[9 - 15\nu - 12 \frac{a^2}{R^2} - \frac{r^2}{R^2} \left(72 - 15\nu - 105 \frac{a^2}{R^2} \right) + 15 \frac{r^4}{R^4} \left(5 - 7 \frac{a^2}{R^2} \right) \right], \quad (C8)$$

$$\sigma_{\theta\theta} = \frac{T}{14 - 10\nu} \frac{a^3}{R^3} \left[9 - 15\nu - 12 \frac{a^2}{R^2} - 15 \frac{r^2}{R^2} \left(1 - 2\nu - \frac{a^2}{R^2} \right) \right], \quad (C9)$$

$$\sigma_{zz} = T \left[1 - \frac{1}{14 - 10\nu} \frac{a^3}{R^3} \left\{ 38 - 10\nu - 24 \frac{a^2}{R^2} - \frac{r^2}{R^2} \left(117 - 15\nu - 120 \frac{a^2}{R^2} \right) + 15 \frac{r^4}{R^4} \left(5 - 7 \frac{a^2}{R^2} \right) \right\} \right], \quad (\text{C10})$$

$$\sigma_{zr} = \frac{T}{14 - 10\nu} \frac{a^3 z r}{R^5} \left[-3(19 - 5\nu) + 60 \frac{a^2}{R^2} + 15 \frac{r^2}{R^2} \left(5 - 7 \frac{a^2}{R^2} \right) \right]. \quad (\text{C11})$$

where a is the hole radius, T is the distant stress applied in the z direction, ν is the Poisson's ratio, $r^2 = x^2 + y^2$ is the cylindrical radial coordinate, $R^2 = r^2 + z^2$ is the spherical radial coordinate, and x, y, z are the Cartesian coordinates.

The displacement distributions were later derived by Goodier [36]:

$$u_r = -\frac{A}{r^2} - \frac{3B}{r^4} + \left[\frac{5 - 4\nu}{1 - 2\nu} \frac{C}{r^2} - 9 \frac{B}{r^4} \right] \cos(2\theta), \quad (\text{C12})$$

$$u_\theta = - \left[\frac{2C}{r^2} + 6 \frac{B}{r^4} \right] \sin(2\theta), \quad (\text{C13})$$

where the constants A, B and C are defined as follows:

$$\frac{A}{a^3} = -\frac{T}{8\mu} \frac{13 - 10\nu}{7 - 5\nu}, \quad \frac{B}{a^5} = -\frac{T}{8\mu} \frac{1}{7 - 5\nu}, \quad \frac{C}{a^3} = -\frac{T}{8\mu} \frac{5(1 - 2\nu)}{7 - 5\nu}. \quad (\text{C14})$$

and μ is the shear modulus.

References

- [1] Das, S., Mathur, S.R., Murthy, J.Y.: An Unstructured Finite-Volume Method for Structure-Electrostatics Interactions in MEMS. Numerical Heat Transfer, Part B: Fundamentals **60**(6), 425–451 (2011) <https://doi.org/10.1080/10407790.2011.628252>
- [2] Cardiff, P., Tuković, Ž., Jasak, H., Ivanković, A.: A block-coupled finite volume methodology for linear elasticity and unstructured meshes. Computers & Structures **175**, 100–122 (2016) <https://doi.org/10.1016/j.compstruc.2016.07.004>
- [3] Castrillo, P., Schillaci, E., Rigola, J.: High-order cell-centered finite volume method for solid dynamics on unstructured meshes. Computers & Structures **295**, 107288 (2024) <https://doi.org/10.1016/j.compstruc.2024.107288>
- [4] Nishikawa, H.: A hyperbolic poisson solver for tetrahedral grids. Journal of Computational Physics **409**, 109358 (2020) <https://doi.org/10.1016/j.jcp.2020.109358>
- [5] Knoll, D.A., Keyes, D.E.: Jacobian-free newton–krylov methods: a survey of approaches and applications. Journal of Computational Physics **193**(2), 357–397 (2004) <https://doi.org/10.1016/j.jcp.2003.08.010>
- [6] Cardiff, P., Tuković, Ž., Jaeger, P.D., Clancy, M., Ivanković, A.: A Lagrangian cell-centred finite volume method for metal forming simulation. International Journal for Numerical Methods in Engineering **109**(13), 1777–1803 (2017) <https://doi.org/10.1002/nme.5345>

<https://onlinelibrary.wiley.com/doi/pdf/10.1002/nme.5345>

- [7] Batistić, I., Cardiff, P., Tuković, Ž.: A finite volume penalty based segment-to-segment method for frictional contact problems. *Applied Mathematical Modelling* **101**, 673–693 (2022) <https://doi.org/10.1016/j.apm.2021.09.009>
- [8] Tuković, Ivanković, A., Karač, A.: Finite-volume stress analysis in multi-material linear elastic body. *International Journal for Numerical Methods in Engineering* **93**(4), 400–419 (2013) <https://doi.org/10.1002/nme.4390> <https://onlinelibrary.wiley.com/doi/pdf/10.1002/nme.4390>
- [9] Jasak, H., Weller, H.G.: Application of the finite volume method and unstructured meshes to linear elasticity. *International Journal for Numerical Methods in Engineering* **48**(2), 267–287 (2000) [https://doi.org/10.1002/\(SICI\)1097-0207\(20000520\)48:2<267::AID-NME884>3.0.CO;2-Q](https://doi.org/10.1002/(SICI)1097-0207(20000520)48:2<267::AID-NME884>3.0.CO;2-Q) <https://onlinelibrary.wiley.com/doi/pdf/10.1002/%28SICI%291097-0207%2820000520%2948%3A2%3C267%3A%3AAID-NME884%3E3.0.CO%3B2-Q>
- [10] Rhie, C.M., Chow, W.L.: Numerical study of the turbulent flow past an airfoil with trailing edge separation. *AIAA Journal* **21**(11), 1525–1532 (1983) <https://doi.org/10.2514/3.8284> <https://doi.org/10.2514/3.8284>
- [11] Demirdžić, I., Muzaferija, S.: Numerical method for coupled fluid flow, heat transfer and stress analysis using unstructured moving meshes with cells of arbitrary topology. *Computer Methods in Applied Mechanics and Engineering* **125**(1), 235–255 (1995) [https://doi.org/10.1016/0045-7825\(95\)00800-G](https://doi.org/10.1016/0045-7825(95)00800-G)
- [12] Jasak, H.: Error analysis and estimation for the finite volume method with applications to fluid flows. PhD thesis, Imperial College London (University of London) (1996)
- [13] Jsvobs, D.A.H.: A Generalization of the Conjugate-Gradient Method to Solve Complex Systems. *IMA Journal of Numerical Analysis* **6**(4), 447–452 (1986) <https://doi.org/10.1093/imanum/6.4.447> <https://academic.oup.com/imajna/article-pdf/6/4/447/2181350/6-4-447.pdf>
- [14] Balay, S., Abhyankar, S., Adams, M.F., Brown, J., Brune, P., Buschelman, K., Dalcin, L., Eijkhout, V., Gropp, W.D., Kaushik, D., Knepley, M.G., McInnes, L.C., Rupp, K., Smith, B.F., Zampini, S., Zhang, H.: PETSc Web page. <http://www.mcs.anl.gov/petsc> (2015). <http://www.mcs.anl.gov/petsc>
- [15] Geuzaine, C., Remacle, J.-F.: Gmsh: A 3-d finite element mesh generator with built-in pre- and post-processing facilities. *International journal for numerical methods in engineering* **79**(11), 1309–1331 (2009) <https://doi.org/10.1002/nme.2579>
- [16] Hitchings, D., Davies, G.A.O., Kamoulakos, A.: Linear Static Benchmarks. International Association for the Engineering Analysis Community & National Agency for Finite Element Methods & Standards (NAFEMS), Glasgow, UK (1987)
- [17] Demirdžić, I., Muzaferija, S., Perić, M.: Advances in computation of heat transfer, fluid flow, and solid body deformation using finite volume approaches. In: W. J. Minkowycz, E.M.S. (ed.)

Advances in Numerical Heat Transfer, Chapter 2, pp. 59–96. Taylor & Francis, ??? (1997)

- [18] Cardiff, P., Tuković, Jasak, H., Ivanković, A.: A block-coupled finite volume methodology for linear elasticity and unstructured meshes. *Computers & Structures* **175**, 100–122 (2016) <https://doi.org/10.1016/j.compstruc.2016.07.004>
- [19] Rohatgi, A.: WebPlotDigitizer. <https://automeris.io>
- [20] Land, S., Gurev, V., Arens, S., Augustin, C.M., Baron, L., Blake, R., Bradley, C., Castro, S., Crozier, A., Favino, M., Fastl, T.E., Fritz, T., Gao, H., Gizzi, A., Griffith, B.E., Hurtado, D.E., Krause, R., Luo, X., Nash, M.P., Pezzuto, S., Plank, G., Rossi, S., Ruprecht, D., Seemann, G., Smith, N.P., Sundnes, J., Rice, J.J., Trayanova, N., Wang, D., Wang, Z.J., Niederer, S.A.: Verification of cardiac mechanics software: benchmark problems and solutions for testing active and passive material behaviour **471**(2184), 20150641 (2015) <https://doi.org/10.1098/rspa.2015.0641>
- [21] Guccione, J.M., Costa, K.D., McCulloch, A.D.: Finite element stress analysis of left ventricular mechanics in the beating dog heart. *Journal of Biomechanics* **28**(10), 1167–1177 (1995) [https://doi.org/10.1016/0021-9290\(94\)00174-3](https://doi.org/10.1016/0021-9290(94)00174-3)
- [22] Zienkiewicz, O.C., Taylor, R.L.: The Finite Element Method vol. 2. Butterworth-heinemann, ??? (2000)
- [23] Areias, P.: Simplas. Portuguese Software Association (ASSOFT). <http://www.simplassoftware.com>.
- [24] Pelteret, J.-P., McBride, A.: The deal.II code gallery: Quasi-Static Finite-Strain Compressible Elasticity. Zenodo (2018). <https://doi.org/10.5281/zenodo.1228964> . <https://doi.org/10.5281/zenodo.1228964>
- [25] Simo, J.C., Armero, F.: Geometrically non-linear enhanced strain mixed methods and the method of incompatible modes. *International Journal for Numerical Methods in Engineering* **33**(7), 1413–1449 (1992) <https://doi.org/10.1002/nme.1620330705> <https://onlinelibrary.wiley.com/doi/pdf/10.1002/nme.1620330705>
- [26] Sá, J.M.A., Areias, P.M.A., Natal Jorge, R.M.: Quadrilateral elements for the solution of elasto-plastic finite strain problems. *International Journal for Numerical Methods in Engineering* **51**(8), 883–917 (2001) <https://doi.org/10.1002/nme.183> <https://onlinelibrary.wiley.com/doi/pdf/10.1002/nme.183>
- [27] Tuković, Ž., Jasak, H.: Updated lagrangian finite volume solver for large deformation dynamic response of elastic body. *Transactions of FAMENA* **31**(1), 55–70 (2007)
- [28] Turek, S., Hron, J.: Proposal for numerical benchmarking of fluid-structure interaction between an elastic object and laminar incompressible flow. In: Bungartz, H.-J., Schäfer, M. (eds.) *Fluid-Structure Interaction: Modelling, Simulation, Optimisation*. Lecture Notes in Computational Science and Engineering, vol. 53, pp. 371–385. Springer, Berlin, Heidelberg (2006). https://doi.org/10.1007/3-540-34596-5_20

- [29] Ferziger, J.H., Peric, M.: Computational Methods for Fluid Dynamics, 3rd edn. Springer, ??? (2002)
- [30] Degroote, J., Bathe, K.-J., Vierendeels, J.: Performance of a new partitioned procedure versus a monolithic procedure in fluid-structure interaction. *Computers & Structures* **87**(11-12), 793–801 (2009) <https://doi.org/10.1016/j.compstruc.2009.01.006>
- [31] Tuković, Ž., Karač, A., Cardiff, P., Jasak, H., Ivanković, A.: OpenFOAM finite volume solver for fluid-solid interaction. *Transactions of FAMENA* **42**(3), 1–31 (2018) <https://doi.org/10.21278/TOF.42301>
- [32] Amestoy, P.R., Duff, I.S., Koster, J., L'Excellent, J.-Y.: A fully asynchronous multifrontal solver using distributed dynamic scheduling. *SIAM Journal on Matrix Analysis and Applications* **23**(1), 15–41 (2001)
- [33] Amestoy, P.R., Buttari, A., L'Excellent, J.-Y., Mary, T.: Performance and Scalability of the Block Low-Rank Multifrontal Factorization on Multicore Architectures. *ACM Transactions on Mathematical Software* **45**, 2–1226 (2019)
- [34] Falgout, R.D., Yang, U.M.: hypre: A library of high performance preconditioners. In: Sloot, P.M.A., Hoekstra, A.G., Tan, C.J.K., Dongarra, J.J. (eds.) *Computational Science — ICCS 2002*, pp. 632–641. Springer, Berlin, Heidelberg (2002)
- [35] Southwell, R.V., Gough, H.J.: Vi. on the concentration of stress in the neighbourhood of a small spherical flaw; and on the propagation of fatigue fractures in “statistically isotropic” materials. *The London, Edinburgh, and Dublin Philosophical Magazine and Journal of Science* **1**(1), 71–97 (1926) <https://doi.org/10.1080/14786442608633614> <https://doi.org/10.1080/14786442608633614>
- [36] Goodier, J.N.: Concentration of stress around spherical and cylindrical inclusions and flaws. *Journal of Applied Mechanics* **1**(2), 39–44 (1933)